Mon. Not. R. Astron. Soc. **265**, 43–71 (1993)

Optical galaxies within 8000 km s^{-1} – I. The density field

Michael J. Hudson★
Institute of Astronomy, Madingley Road, Cambridge CB3 0HA

Accepted 1993 May 6. Received 1993 April 22; in original form 1992 November 25

ABSTRACT

The density field of optical galaxies to a depth of 8000 km s^{-1} over 67 per cent of the sky is determined using the UGC and ESO catalogues. The reconstruction method compensates for the varying completeness of the redshift data and for the galaxies that are not selected in the catalogues. The optical density field is dominated by supercluster complexes with dimensions in excess of 6000 km s^{-1}. The most prominent of these are Perseus–Pisces and Centaurus–Hydra–Virgo–Pavo. The same complexes are seen in maps of *IRAS* galaxies, but the contrast of the optical maps is higher by a factor of 1.35 ± 0.16 when measured in 2500 km s^{-1} cells. By comparing the overdensity of galaxies in the Virgo supercluster to Virgo infall and assuming that mass follows light, we obtain $\Omega = 0.20^{+0.30}_{-0.15}$. The 'Great Attractor Region' covered by Dressler's Supergalactic Plane Survey is overdense to 6000 km s^{-1}, well beyond the Cen 30 cluster. However, unless there is a massive supercluster hidden in the zone of avoidance, this region is not sufficiently overdense for it to be identified with the Great Attractor inferred from $D_n - \sigma$ and Tully–Fisher peculiar velocities. Furthermore, within the Centaurus–Hydra–Virgo–Pavo complex, the density field peaks close to the Cen 30 cluster, which suggests that large-scale streaming motions may be better described by a weak 200 ± 150 km s^{-1} infall centred near Cen 30, plus a bulk dipole motion of 400 ± 150 km s^{-1} in the CMB frame.

Key words: surveys – galaxies: clustering – galaxies: distances and redshifts – cosmology: observations – dark matter – large-scale structure of Universe.

1 INTRODUCTION

With the advent of large redshift surveys and well-selected galaxy catalogues, it has become possible to obtain reliable maps of the local Universe as traced by galaxies. By assuming some relation between the observed light and the underlying mass, one can use such maps to predict the motion of the Local Group and the infall into nearby superclusters. The latter can then be compared to infall determinations from Tully–Fisher or $D_n - \sigma$ peculiar velocities. Whereas for statistical purposes, such as galaxy clustering, it is sufficient to survey only part of the sky, when predicting streaming motions it is necessary to map the density field over as much of the sky as possible, and to sufficient depth to account for the motions of the galaxies of interest. The density field to a depth of 4000 km s^{-1} was calculated from the Revised Shapley–Ames Catalogue (Sandage & Tammann 1981) by Yahil, Sandage & Tammann (1980) with the aim of determining the overdensity of galaxies in the Local Supercluster. Davies & Huchra (1982) used the CfA1 redshift survey (at high latitudes) for a similar purpose. The Nearby Galaxies Catalogue (Tully 1988) has a depth of 3000 km s^{-1}. Recently, Shaya, Tully & Pierce (1992) have used the density field from this catalogue directly to predict the peculiar motions of galaxies within this volume. These surveys do not, however, have sufficient coverage to account for the motion of the Local Group in the frame of the cosmic microwave background (hereafter CMB), and, in particular, the volumes mapped do not include the Hydra–Centaurus/Great Attractor region, which may have a significant effect on the motion of the Local Group and nearby galaxies (Shaya 1984; Lilje, Yahil & Jones 1986; Lynden-Bell et al. 1988, hereafter 7S).

Two groups have used *IRAS* galaxies as tracers of the density field. Strauss et al. (1990, 1992c) have completed a redshift survey of a sample of 2658 *IRAS* galaxies with 60-μm flux brighter than 1.936 Jy (we refer to this as the '2-Jy' sample). This survey has a depth of at least 8000 km s^{-1} and covers 88 per cent of the sky. Assuming simple biasing and a value of Ω, they self-consistently transformed from redshift space to distance space (Yahil et al. 1991, hereafter YSDH) and made predictions of the peculiar velocity of the Local

★ Present address: Department of Physics, University of Durham, South Road, Durham DH1 3LE.
E-mail: M.J.Hudson@durham.ac.uk.

Group (Strauss et al. 1992b). A deeper but sparser sample of *IRAS* galaxies, the one-in-six 0.6-Jy QDOT survey, has been used in similar studies (Rowan-Robinson et al. 1990, hereafter RR90; Saunders et al. 1991, hereafter S91; Kaiser et al. 1991). *IRAS* samples have the advantage that *IRAS* fluxes are uniform across the sky, and are not affected by foreground absorption due to our Galaxy. However, a serious concern with these samples is that they do not include the elliptical galaxies found predominantly in the cluster cores. Furthermore, *IRAS* density fields are noisy nearby due to the sparseness of the samples and to the fact that *IRAS* flux is not well correlated with mass.

In this paper, we determine the density field of optically selected galaxies within 8000 km s^{-1}. Our density field includes the region of the proposed Great Attractor (7S; Faber & Burstein 1988) and is expected to be of sufficient depth to account for $\gtrsim 80$ per cent of the motion of the Local Group (Lynden-Bell, Lahav & Burstein 1989; RR90; but see also Strauss et al. 1992b). Ideally, the optical density field would be determined from a complete redshift survey, drawn from a uniform, all-sky optical catalogue. Instead, we must use the existing catalogues and redshift data, which have varying selection criteria across the sky and in depth. Consequently, Sections 2–5 describe the sample selection and corrections to the data in some detail. Sections 6–9 present maps of the density field and results. We now summarize these sections briefly. We discuss the diameter systems and selection criteria of our merged catalogue in Section 2. To determine the density field in three dimensions, we use the published wide-angle redshift surveys and redshift compilations. The redshift sample is described in Section 3. In Section 4 we determine the completeness of the redshift sample relative to the catalogues. In Section 5 we describe the weighting scheme that is used to correct for incompleteness of the redshift sample and the diameter limit, and so determine the underlying density field. We also describe the iterative method used to transform the optical density field self-consistently from pseudo-3D 'redshift space' to 'distance space'. We present maps of the density field in Section 6. In Section 7 we compare the density fields of early- and late-type galaxies, and in Section 8 we compare the optical density field with the density field of *IRAS* galaxies. Finally, in Section 9, we discuss the major superclusters within the local volume, compare the predicted infall to the observations, and discuss the implications of our results for determinations of Ω and studies of large-scale streaming motions.

Throughout this paper, we express all distances, r, in units of km s^{-1}. Velocities, $v = cz$, are converted from heliocentric redshifts to the frame of the barycentre of the Local Group by adding 300 sin l cos b throughout.

2 THE CATALOGUE

Although magnitude limits are commonly used as selection criteria, magnitude-limited catalogues of optical galaxies of sufficient depth [such as the catalogue of Zwicky (1961–68), hereafter CGCG] cover only the northern sky. The Uppsala General Catalogue of Galaxies (hereafter UGC: Nilson 1973) and The ESO–Uppsala Survey of the ESO(B) Atlas (hereafter ESO: Lauberts 1982) are diameter-limited, and between them cover most of the sky. In a previous paper (Hudson & Lynden-Bell 1991, hereafter HL-B), we investigated the completeness of the UGC and ESO catalogues, and determined the distribution of metric diameters, the diameter function.

The UGC and ESO catalogues cover the declination ranges Dec. $\geq -25^{\circ}.5$ and Dec. $\leq -17^{\circ}.5$ respectively. The existing catalogues that cover the 'missing' equatorial strip between UGC and ESO are (a) the Morphological Catalogue of Galaxies (Vorontsov-Velyaminov & Krasnogorskaya 1962; Vorontsov-Velyaminov & Arkhipova 1963–68), which is magnitude-limited but has poor positions, diameters and variable completeness, and (b) the Extension to the Southern Galaxies Catalogue (Corwin & Skiff, in preparation), which is complete only for angular diameters larger than 2 arcmin. Furthermore, there are no uniform redshift surveys in this strip. This makes it difficult to transform the diameters of these galaxies to the UGC or ESO systems. Due to the sparseness of the data, and the large systematic uncertainties introduced by the incompleteness and diameter systems, we prefer to treat this small area (7.5 per cent of the sky) in the same way as the zone of avoidance (21 per cent of the sky), as described in Section 5.3 below.

2.1 Morphological selection

In the following analysis, we have used the computer-readable versions of the UGC and ESO catalogues kindly provided by D. Burstein. The ESO version contains all entries of the ESO catalogue coded by 'G', 'IG' or 'G?'. Throughout this work we will treat early- and late-type galaxies separately. The early-type ('E + S0') sample includes all galaxies coded by Burstein as E to S0 or as 'Compact' ($T < 0$). The 'S + Irr' sample consists of galaxies with types coded as S0/a to Irr, or as 'S...' or 'Dwarf' ($0 \leq T \leq 10$). Both the ESO and UGC catalogues include entries for multiple systems (pairs, groups and clusters). For multiple systems, the catalogue diameter refers to the diameter of the system, which may be up to an order of magnitude larger than the diameters of individual galaxies. We therefore exclude multiple systems, as well as peculiar and unclassified galaxies, from the samples in this work.

2.2 Corrections to visual diameters

Our method is based on UGC and ESO major diameters, θ. Both the UGC and ESO diameters are *visual* determinations from plates of the 'maximum extent of features which may be described as belonging to the object' (UGC; ESO). Linear transformations from the UGC and ESO visual diameters to isophotal diameters (at 25 B mag arcsec^{-2}), θ_{25}, were obtained by Paturel et al. (1991), and these were adopted by de Vaucouleurs et al. (1991, hereafter RC3; but see also Cornell et al. 1987, who found a non-linear relationship between UGC and isophotal diameters). We adopt the declination correction to ESO diameters of Paturel et al. (1987, their equation 2a), then use the RC3 transformation to scale the ESO diameters. We then scale the UGC diameters such that the UGC and ESO diameter functions match (see Section 5.1). We make no correction for inclination, as recent studies indicate that UGC (Burstein, Haynes & Faber 1991; Choloniewski 1991) and ESO (Huizinga & van Albada 1992) *visual* diameters are independent of inclination.

Surface brightness was corrected for absorption [using a computer-readable version of the reddening maps of Burstein & Heiles (1982), kindly provided for us by D. Burstein, and assuming $A_B = 4E(B-V)$]; k-corrections from de Vaucouleurs, de Vaucouleurs & Corwin (1976, hereafter RC2); and cosmological $(1+z)^4$ dimming. A diameter correction factor was then calculated for a given surface brightness dimming by adopting a model of the surface brightness profile. For spirals and later types, we have found that ESO galaxies have a mean central surface brightness $\mu_0^B \simeq 21.5$ B mag arcsec^{-2}. We assume that the visual diameters correspond to the 25.5 B mag arcsec^{-2} isophote (Cornell et al. 1987; Paturel et al. 1987, 1991) and that they are exponential discs. The diameters of E+S0s were similarly adjusted by assuming that they follow an $R^{1/4}$ law with mean surface brightness within the effective radius $\langle\mu\rangle_e \simeq 21.5$ B mag arcsec^{-2} (Sandage & Perelmuter 1990). Diameters were also corrected for cosmological effects via the angular diameter distance formula with $q_0 = 1/2$ (Weinberg 1972). In the final sample, most corrections are of the order of a few per cent, and the maximum correction is a factor of 1.56.

2.3 Completeness of the catalogues

HL-B investigated the completeness of the UGC and ESO catalogues, and determined that the latter is complete at $\theta > 1.35$ arcmin. The UGC number counts were found to rise less quickly than expected in a homogeneous universe. HL-B interpreted this as incompleteness in the UGC catalogue, and modelled the raw counts as $N(\theta_{UGC})\,d\theta_{UGC} \propto C(\theta_{UGC})\,\theta_{UGC}^{-4}$, where $C(\theta_{UGC})$ is the completeness function. This completeness function was found to fit the counts in both the North and South Galactic Caps and the counts of both early- and late-type galaxies. Using this function, the completeness is 64 per cent at 1.2 arcmin, rising to 78 per cent at 1.4 arcmin and to 100 per cent at diameters larger than 1.65 arcmin. It is, however, also possible that the fall-off in number counts is due to non-linearities in the diameter scale at $\theta < 1.65$ arcmin in the sense that the visual diameters of smaller galaxies are effectively measured at a brighter isophote (as found by Cornell et al. 1987, but not by Paturel et al. 1991). In either case, the necessary correction is in the same sense: small galaxies should be assigned greater weight, either to compensate for those missed or to compensate for their underestimated diameters. As we do not have the photometric data to resolve this question, we adopt the UGC completeness correction of HL-B.

2.4 The final catalogue

The final merged catalogue is obtained by limiting UGC and ESO to raw diameters greater than 1.15 and 1.35 arcmin respectively, at which limits the catalogues have similar depths. The morphological selection criteria are as given above. Fig. 1 shows all galaxies that meet these criteria. At this stage, we exclude from our final catalogue all galaxies with $|b| < 10°$. In the ESO catalogue, there are too few measured redshifts to allow a determination of the density field in a small region near the Galactic Centre ($350° < l < 30°$, $b > -30°$, Dec. $< -17\overset{\circ}{.}5$) and in a region at RA $< 9^h$, $b > 10°$, Dec. $< -17\overset{\circ}{.}5$. These regions and all galaxies in them were also excluded from the merged catalogue. The area on the sky covered by the merged catalogue is referred to as the 'catalogued' area and the remainder as the 'masked' area. We refer to this merged catalogue of 12 349 galaxies as 'U+E', and use this as our two-dimensional catalogue throughout.

3 REDSHIFT DATA

3.1 Redshift compilations and identifications

Our primary sources of redshifts are the compilations of Huchra (1990 ZCAT) and Fairall & Jones (1991, Southern Redshift Catalogue, hereafter SRC). The ZCAT is an all-sky compilation, the 1990 version of which lists published redshifts, positions, names and occasionally diameters and UGC identifications, amongst other parameters. The SRC covers only the southern sky and gives redshifts, positions, and ESO or other identifications. ZCAT and SRC compile all published redshifts to 1990 and 1991, respectively, and both include references to the original published source of each redshift.

The identifications with UGC or ESO galaxies in these publications are not complete. To complete the identifications, we searched ZCAT and SRC for all entries with positions within 6 arcmin of each UGC or ESO galaxy. Where the positions and diameters and/or UGC or ESO identifications matched, the identification was assigned automatically. Other cases (e.g. diameter mismatch or more than one galaxy within 1 arcmin) were inspected, and the redshifts quoted or identifications made in other catalogues, such as the PGC (Paturel et al. 1989) or the NED data base (Helou et al. 1991), were used.

3.2 Uniform redshift surveys

There are five wide-angle uniform redshift surveys that are useful for our purposes. In the northern celestial hemisphere (UGC), these are the following.

CfA1, the first Centre for Astrophysics survey (Huchra et al. 1983), covers Dec. $\geq 0°$, $b \geq 40°$ and Dec. $\geq -2\overset{\circ}{.}5$, $b \leq -30°$ and was drawn from the CGCG to a magnitude limit $m_{Zw} \leq 14.5$ mag.

CfA2, the first slice of the second CfA survey (Huchra et al. 1990), covers $8^h \leq$ RA $\leq 17^h$, $26\overset{\circ}{.}5 \leq$ Dec. $\leq 32\overset{\circ}{.}5$ and was drawn from the CGCG to a magnitude limit $m_{Zw} \leq 15.5$ mag.

PP (Giovanelli & Haynes 1985; Giovanelli et al. 1986b) covers $21^h \leq$ RA $\leq 4^h$, $21\overset{\circ}{.}5 \leq$ Dec. $\leq 33\overset{\circ}{.}5$ and consists of late-type galaxies drawn from the CGCG and UGC catalogues.

In the southern celestial hemisphere (ESO), the surveys used are the following.

SSRS, the Southern Sky Redshift Survey (da Costa et al. 1988; da Costa et al. 1991), covers the region Dec. $\leq -17\overset{\circ}{.}5$, $b \leq -30°$ and was drawn from the ESO catalogue with 'face-on' corrected angular diameters larger than 1.26 arcmin.

SPS, the Supergalactic Plane Survey (Dressler 1991, hereafter SPS), covers the 'Great Attractor Region' ($290° \leq l \leq 350°$, $-30° \leq b \leq 45°$) and has the same selection criterion as SSRS.

CfA1 and CfA2 were extracted from ZCAT by discarding the redshifts of all galaxies within their areas with m_{Zw}

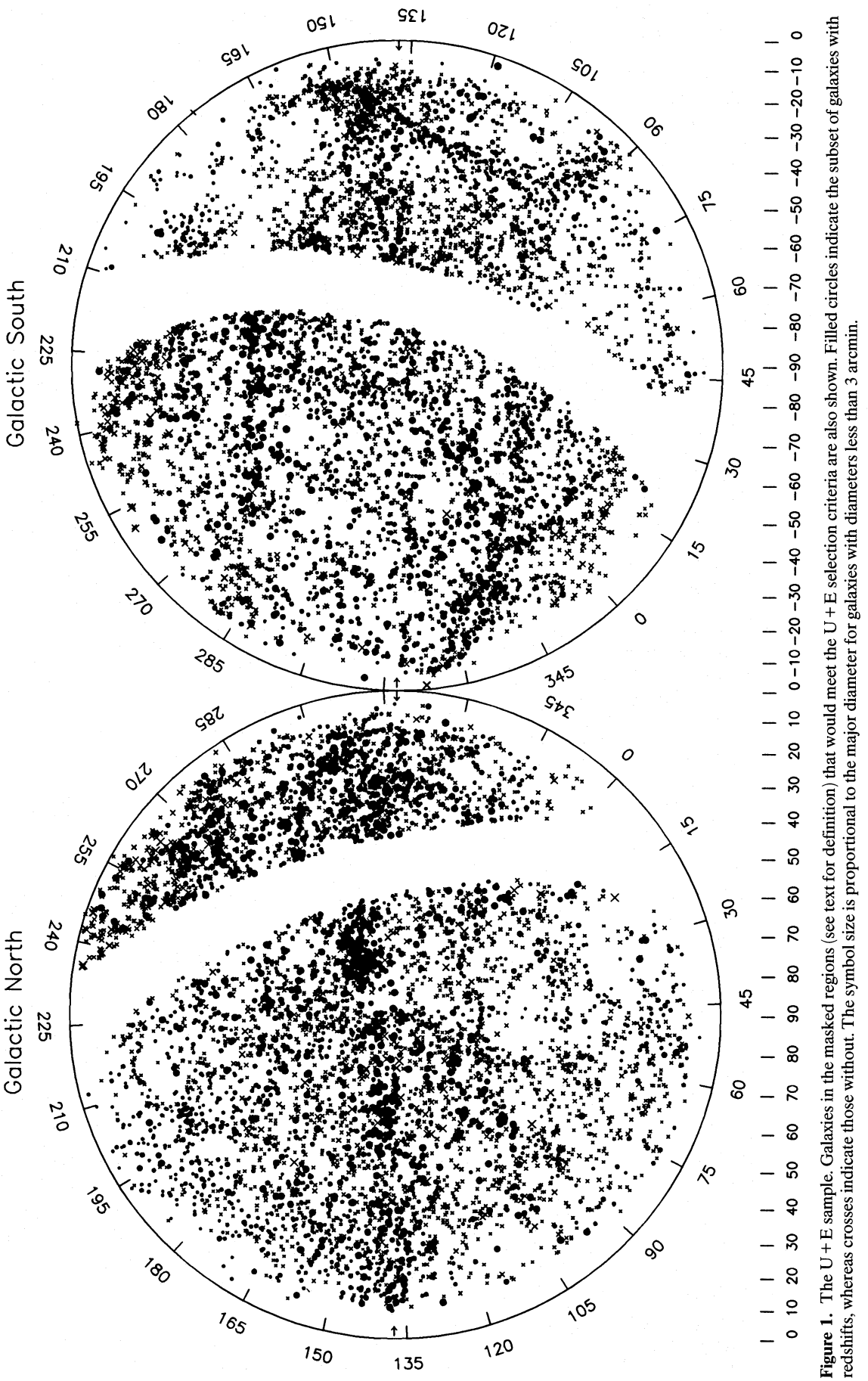

Figure 1. The U + E sample. Galaxies in the masked regions (see text for definition) that would meet the U + E selection criteria are also shown. Filled circles indicate the subset of galaxies with redshifts, whereas crosses indicate those without. The symbol size is proportional to the major diameter for galaxies with diameters less than 3 arcmin.

greater than 14.5 or 15.5 mag respectively. PP is nearly complete to the adopted diameter limits; we used all ZCAT galaxies in UGC within the PP area. We obtained the computer-readable versions of SSRS and SPS from the authors.

3.3 The final redshift subsample

We refer to the combined area covered by the uniform redshift surveys described above as the 'surveyed' area and refer to the remainder of the catalogued area as the 'unsurveyed' area. Note that the surveyed area is mainly at high galactic latitudes.

Our weighting scheme requires that we know redshift completeness as a function of diameter and position on the sky. In the final 'redshift subsample', *within the surveyed area*, we use only the subset of galaxies that are in one of the redshift surveys and in U+E. The advantage of this cut is that the redshift completeness within the surveyed area is uniform. This is particularly important in the surveyed areas, because these areas will be used to determine the diameter functions (see Section 5.1). Although some redshifts are discarded by this cut (and thus, in principle, information is lost), in practice the numbers involved are small: the average completeness is reduced by only ≈ 5 per cent. In the unsurveyed area, we use all redshifts obtained from ZCAT or SRC that are in U+E. The galaxies in the redshift subsample are indicated by field circles in Fig. 1; those without redshifts are indicated by crosses. The total number of redshifts in the subsample is 6747 and so the overall completeness is 54 per cent. The statistics for the U+E catalogue and the redshift sample are given in Table 1. Fig. 2 is a histogram of all velocities in the redshift subsample.

Finally, we note that updated versions of ZCAT have been released since the version used here. However, an examination of the 1992 version indicates that, had it been used instead, only $\simeq 300$ redshifts would be added to the redshift subsample, increasing the overall redshift completeness by $\lesssim 5$ per cent.

4 REDSHIFT COMPLETENESS

On average, the completeness of the unsurveyed areas (1786 redshifts from 3787 galaxies, or 47 per cent) is not that much lower than in the surveyed areas (4960 redshifts from 8650 galaxies, or 57 per cent). The difficulty in determining the

Table 1. Redshift statistics for the U+E sample.

	UGC		ESO		S+Irr		E+S0		**U+E**	
	N	%	*N*	%	*N*	%	*N*	%	**N**	**%**
Total in catalogue	7189		5250		10384		2055		**12439**	
With redshifts	3500	49	3247	62	5387	52	1360	66	**6747**	**54**
($v_{LG} \leq 8000$ km s^{-1})	3217		2766		4794		1189		**5983**	

Notes. The UGC and ESO samples are subsets of the U+E catalogue, with selection criteria described in the text. The percentages are the redshift completeness.

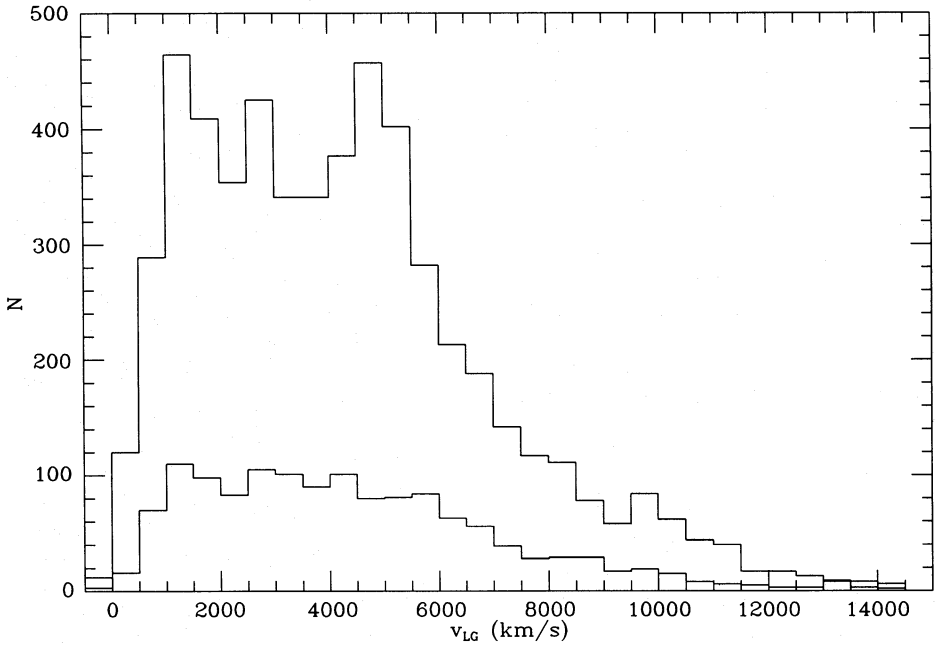

Figure 2. Velocity histogram for the redshift subsample. The distribution of velocities of S+Irr galaxies is shown in the upper histogram, whereas that of E+S0 galaxies is shown in the lower histogram.

completeness arises primarily from its variation across the sky, which may sometimes be very rapid (e.g. at the edges of redshift surveys or around clusters). Simple schemes (e.g. measurement of the completeness within circles on the sky) tend to smooth over these rapid variations in completeness. We may, however, use our a priori knowledge of the major redshift sources in ZCAT and SRC to identify these boundaries on the sky. Our approach to determining the redshift completeness over the unsurveyed area is to break the sky up into a patchwork of small regions, called 'zones'. We then assume that within each zone the completeness is independent of the position on the sky, $\hat{\boldsymbol{r}}$. The boundaries of these zones are initially selected 'by hand', using our knowledge of the redshift surveys and nearby clusters, and then adjusted by statistical tests as described below.

4.1 Completeness 'zones'

Each redshift survey is uniformly selected to a magnitude or 'face-on' diameter limit over its area. Each survey was therefore taken as a zone, with the following exceptions. The SPS was subdivided into northern galactic and southern galactic zones. With regard to the CfA1 survey, it has been shown that Zwicky magnitudes vary systematically by 0.1–0.2 mag between volumes of the CGCG and around Virgo (Kron & Shane 1976; Giovanelli & Haynes 1984; Auman, Hickson & Fahlman 1989). We therefore subdivide the CfA1 region into zones corresponding to volumes 1–4 (excluding the CfA2 strip), volumes 5 and 6 (in the galactic south), and the nine plates centred on Virgo.

In the unsurveyed area, redshifts in the sample were obtained from a number of sources, such as, for example, narrow-angle surveys of given regions [e.g. da Costa et al. (1987) in Hydra–Centaurus], studies of nearby clusters [e.g. Richter, Materne & Huchtmeier (1982) and Richter (1987) in Hydra], and studies of given classes of galaxy [e.g. Bothun et al.'s (1985) survey of low surface brightness galaxies]. In an initial attempt to define regions of approximately uniform completeness, we searched the reference lists of ZCAT and SRC and compiled a list of all references that had contributed more than 10 redshifts to the unsurveyed area. The original references usually indicated the areas on the sky surveyed, and these delineated the initial boundaries of the 'zones' (but here we did not discard additional redshifts that might have been obtained by other workers since the publication of the original survey). For example, da Costa et al. (1987) surveyed two regions in Hydra–Centaurus: $13^{\rm h} \le \mathrm{RA} \le 14^{\rm h}$, $-30° \le \mathrm{Dec.} \le -25°$ and $11^{\rm h} \le \mathrm{RA} \le 12^{\rm h}$, $-33° \le \mathrm{Dec.} \le -27°$. The former region does not concern us, as it is within the SPS area. However, the latter region, excluding the small overlap with SPS, would delineate a zone. Other features, such as the Arecibo declination limit at Dec. $\simeq 38°$, also provided obvious zone boundaries.

A further check for non-uniformity was made by subdividing each zone in two, and testing whether the average completeness of the two subzones was significantly different from the average completeness of the original zone. [The adopted significance level was 1 per cent, because variations in the mean diameter (depth) of the two subzones can yield different values for the diameter-averaged completeness, even for the same completeness function.] If a significant difference was found, then the two subzones were adopted as new zones. (However, in cases where there were too few galaxies, typically less than 10, within one of the subzones to measure the completeness function, the zone was not subdivided.) The process was repeated until no further subdivisions were necessary. We tested subdivisions along lines of RA, Dec., l and b and in circles of varying radii separating clusters from the surrounding 'field'. The list of candidate cluster centres was compiled from the literature [Rood's (1991) redshift compilation of Abell clusters, Schmidt's (1986) lists and the groups of 7S], and from a cluster sample determined directly from the redshift subsample by a percolation algorithm described below (Section 5.4). In some cases, we found a second annular zone around certain clusters where the completeness was lower than in the 'core', but still higher than in the surrounding field.

The entire procedure as described above was carried out separately for the E+S0 subsample and the S+Irr subsample, as the completeness of each can be quite different (e.g. radio telescopes generally do not detect early-type galaxies). We identify 41 S+Irr field zones and 16 S+Irr cluster zones, whose boundaries are described in Tables 2 and 3 and shown on the sky in Fig. 3; and 26 E+S0 field zones and 8 E+S0 cluster zones as described in Tables 4 and 5 and in Fig. 4.

4.2 Completeness functions

In each zone, the completeness of the redshift sample relative to the catalogue as a function of raw (uncorrected) diameter was modelled using the functional form of HL-B,

$$S(\theta) = \begin{cases} S_1 + S_2\theta^{-2} + S_3\theta^{-4} & \theta_0 \le \theta \le 3', \\ 1 + S_4\theta^{-2} + S_5\theta^{-4} & \theta > 3', \end{cases} \tag{1}$$

where θ_0 is the minimum diameter and

$$\begin{aligned} S_4 &= 18(S_1 - 1) + S_2, \\ S_5 &= -81(S_1 - 1) + S_3. \end{aligned} \tag{2}$$

To obtain the parameters of best fit, we maximize the log likelihood

$$\ln \mathscr{L} = \sum_{i \in \text{redshifts}} \ln S(\theta_i) + \sum_{j \in \text{no redshifts}} \ln[1 - S(\theta_j)] \tag{3}$$

with respect to S_1, S_2 and S_3, prohibiting fits that have $S < 0$ or $S > 1$ at any $\theta \ge \theta_0$. To assess the goodness of fit, the data are binned into 12 diameter bins. Given $S(\theta)$, we calculate the expected number of galaxies with redshifts for each bin and errors from the binomial probability. The calculated χ^2 can then be compared to that expected for $12 - 3 = 9$ degrees of freedom.

Tables 6 (S+Irr field), 7 (S+Irr cluster) and 8 (E+S0 field and cluster) give, for each zone, the total number of U+E galaxies, the number with redshifts, the mean velocity, the mean diameter, the average completeness, the selection function parameters and the χ^2 of the fit (9 degrees of freedom). Although the fits of some zones (e.g. some CfA1 zones) are formally unacceptable, it is not clear whether any other smooth curve would improve the fit.

Table 2. S + Irr field zones.

No.	Zone Name	Dec. min	Dec. max	R.A. min	R.A. max	b min	b max	l min	l max	Excluding Zones
1	And/Cas	35	—	22^h	4^h	—	-10	—	—	Per, Lac
2	Ant_E	-40	-30	10^h10^m	10^h50^m	—	—	—	—	—
3	Ant_W	-40	-30	10^h	10^h10^m	—	—	—	—	—
4	Aur	38	65	—	—	10	15	—	—	—
5	Cam_E	65	90	4^h	10^h	20	40	—	—	—
6	Cam_W	65	90	4^h	—	10	20	—	—	—
7	Car	—	-45	—	—	-20	-10	—	290	—
8	Cen_W	—	-30	10^h	—	10	—	—	290	Hya_E, Ant_E, Ant_W
9	Cep	—	90	22^h	4^h	10	—	—	—	—
10	CfA1_V1	0	14.5	—	—	40	—	—	—	CfA1_Vir
11	CfA1_V2	14.5	26.5	—	—	40	—	—	—	CfA1_Vir
12	CfA1_V3	32.5	56.5	—	—	40	—	—	—	—
13	CfA1_V4	56.5	—	—	—	40	—	—	—	—
14	CfA1_V5+6	-2.5	21.5	—	—	—	-30	—	—	—
15	CfA1_Vir	2.5	20.5	11^h52^m	13^h04^m	—	-30	—	—	—
16	CfA2	26.5	32.5	8^h	17^h	—	-30	—	—	—
17	Cnc_E	-2.5	38	8^h	—	25	40	—	—	CfA2
18	Cnc_W	-2.5	—	8^h	—	—	25	—	—	—
19	Col	-45	-17.5	—	—	-30	-10	—	—	—
20	Crt	-27	-17.5	11^h	—	—	—	—	290	—
21	Del	-2.5	—	—	23^h	-30	-10	—	—	PP(I+II), Lac, And/Cas
22	Dra	38	—	10^h	22^h	10	40	—	—	—
23	Gem	-2.5	38	—	8^h	10	—	—	—	—
24	Her	23.5	30	—	—	10	40	—	—	CfA2
25	Her/Oph	10	23.5	—	—	10	40	—	—	—
26	Her_N	30	38	—	—	10	40	—	—	CfA2
27	Hya_E	-33	-27	11^h	—	—	—	—	290	—
28	Hya_W	-30	-17.5	10^h	11^h	—	—	—	—	—
29	Lac	33.5	*	22^h	24^h	—	-10	—	—	PP(I+II)
30	Lyn_N	55	65	—	—	15	40	—	—	—
31	Lyn_S	38	55	—	—	15	40	—	—	—
32	Oph	-2.5	10	—	—	10	40	—	—	—
33	PP(I+II)	21.5	33.5	21^h	4^h	—	-10	—	—	—
34	Per	30	*	0^h	4^h40^m	—	—	—	—	PP(I+II)
35	Pyx	—	-17.5	9^h	10^h	10	—	—	—	—
36	SPS_($b<0$)	—	—	—	—	-30	-10	290	350	—
37	SPS_($b>0$)	—	-17.5	—	—	10	45	290	350	—
38	SSRS	—	-17.5	—	—	—	-30	—	—	—
39	Tau	-2.5	30	—	—	10	30	—	—	PP(I+II)
40	UGC_S	-2.5	0	—	—	40	—	—	—	—
41	Vol/Pic	-75	-45	—	—	-30	-20	—	290	—

*The upper boundary of the Perseus–Pisces ridge as in fig. 4 of Giovanelli, Haynes & Chincarini (1986a).

4.3 Tests of the completeness functions

We wish to know whether our division of the sky is adequate in accounting for the variations in completeness in the unsurveyed areas. We can test this by checking whether the galaxies in the redshift subsample are more clustered than those in U + E. This can be measured by computing angular correlation functions as follows. Galaxies in the redshift subsample are given a weight of $1/S(\theta, \hat{\boldsymbol{r}})$ and are denoted by the subscript (z), whereas 'c' denotes a galaxy (unweighted) in the U + E catalogue. We also generate a set of points with positions chosen at random within the area and denote these by the subscript 'r'. Let $N_{zz}(\Theta)$, $N_{zc}(\Theta)$, $N_{cc}(\Theta)$, $N_{zr}(\Theta)$ and $N_{cr}(\Theta)$ be pair counts of the objects denoted by their subscripts, within an angular annulus between Θ and $\Theta + d\Theta$. Now, the usual angular autocorrelation function is

$$\omega_{cc}(\Theta) = \frac{N_{cc}(\Theta)\, n_r}{N_{cr}(\Theta)\, n_c} - 1, \tag{4}$$

where n is the average surface density. We are interested, however, in the *excess* correlation of the redshift subsample against U + E. To determine this we calculate the correlation of the weighted redshift subsample compared, not to a random distribution, but to the underlying catalogue. Specifically, we calculate

$$\omega_{zz/zc}(\Theta) = \frac{N_{zz}(\Theta)\, n_c}{N_{zc}(\Theta)\, n_z} - 1 = \frac{\omega_{zz} + 1}{\omega_{zc} + 1} - 1. \tag{5}$$

If the redshift subsample is drawn randomly from U + E with probability $S(\theta, \hat{r})$, then $\omega_{zz} = \omega_{zc} = \omega_{cz} = \omega_{cc}$, and so the excess correlation $\omega_{zz/zc} = 0$. In Fig. 5, we show the excess correlation, $\omega_{zz/zc}$ (solid circles), and the autocorrelation of the redshift subsample, ω_{zz} (open circles), for the UGC and ESO unsurveyed areas. The excess correlation is negligible on scales larger than 1°. On smaller scales, the non-zero excess correlation indicates that, after the correction for incompleteness described above, galaxies with redshifts are more clustered than those in the underlying catalogue. This implies that the zones do not accurately track very small-scale variations in completeness. However, as we will ultimately smooth the density field on scales of 500 km s^{-1} (i.e. > 3°.5 within a distance of 8000 km s^{-1}), this clustering does not concern us here.

As a further check, in Fig. 6 we compare the surface number density of galaxies in U + E to those in the redshift subsample weighted by $1/S(\theta, \hat{r})$. The surface densities are constructed using the spherical harmonic components with $l \leq 20$ (Scharf et al. 1992). This corresponds to an effective smoothing scale of ~9°. The noise level is higher in the weighted redshift map, where it is approximately 0.4 times

Table 3. S + Irr cluster zones.

Zone No.	Zone Name	Cluster Centre l	Cluster Centre b	Radius	Within Field Zone
42	A262_core	136°.6	−25°.1	0°.5	Per
43	A539	195.7	−17.7	5.0	Tau
44	Cnc_clus	202.7	28.6	4.0	Cnc_E
45	0041+51_core	121.7	−12.1	4.0	And/Cas
46	0337+40	154.4	−12.0	2.0	Per
47	0454+02	197.0	−24.4	3.0	Tau
48	1726+59	87.6	33.8	4.0	Dra
49	0608−22	228.4	−18.4	1.5	Col
50	A262_halo	136.6	−25.1	4.0	Per
51	A347	141.2	−17.6	6.0	Per
52	Per_clus	150.4	−13.4	0.5	Per
53	Hya_clus	269.6	26.5	2.0	Hya
54	AWM7	146.3	−15.7	5.0	Per
55	0041+51_halo	121.7	−12.1	10.0	And/Cas
56	2030+11	54.6	−16.8	1.5	Del
57	7S053	286.0	43.0	2.0	Crt

Table 5. E + S0 cluster zones.

Zone No.	Zone Name	Cluster Centre l	Cluster Centre b	Radius	Within Field Zone
27	A262	136°.6	−25°.1	3°.0	PP_ridge
28	A347	141.2	−17.6	1.5	PP_ridge
29	Pers_clus	150.4	−13.4	0.5	PP_ridge
30	A539	195.7	−17.7	10.0	Del-Ori
31	Psc_clus	126.7	−30.3	8.0	PP_ridge
32	Cnc_clus	202.7	28.6	6.0	Cnc/Lyn
33	A634	159.4	33.6	10.0	Cnc/Lyn
34	7S100	199.7	−28.9	1.5	Del-Ori

Table 4. E + S0 field zones.

No.	Zone Name	Dec. min	Dec. max	R.A. min	R.A. max	b min	b max	l min	l max	Excluding Zones
1	Ant	-42	-30	10^h	10^{h}50^m	—	—	—	—	—
2	Cam	60	90	4^h	8^h	10	—	—	—	—
3	Car	—	-35	—	—	-30	-10	—	290	—
4	Cen_W	—	-30	10^{h}10^{10}	—	10	—	—	290	Hya_E, Ant
5	Cep+Cam_E	60	90	22^h	10^h	10	—	—	—	Cam
6	CfA1_V1	0	14.5	—	—	40	—	—	—	CfA1_Vir
7	CfA1_V2	14.5	26.5	—	—	40	—	—	—	CfA1_Vir
8	CfA1_V3	32.5	56.5	—	—	40	—	—	—	—
9	CfA1_V4	56.5	—	—	—	40	—	—	—	—
10	CfA1_V5	-2.5	21.5	—	—	—	-30	—	—	—
11	CfA1_V6	21.5	—	—	—	—	-30	—	—	—
12	CfA1_Vir	2.5	20.5	11^{h}52^m	13^{h}04^m	—	-30	—	—	—
13	CfA2	26.5	32.5	8^h	17^h	—	-30	—	—	—
14	Cnc/Lyn	-2.5	60	8^h	—	—	40	—	—	CfA2
15	Col	-35	-17.5	—	—	-30	-10	—	—	—
16	Del-Ori	-2.5	-	—	—	-30	-10	—	—	PP_ridge
17	Dra-Oph	-2.5	—	10^h	22^h	10	40	—	—	—
18	Gem	-2.5	60	—	8^h	10	—	—	—	—
19	Hya_E	-33	-17.5	11^h	—	—	—	—	290	—
20	Hya_W	-30	-17.5	10^{h}10^m	11^h	—	—	—	—	—
21	PP_ridge	*	*	22^h	5^h	-30	-10	—	—	—
22	Pyx	—	-17.5	9^h	10^{h}10^m	10	—	—	—	Ant
23	SPS_(b < 0)	—	—	—	—	-30	-10	290	350	—
24	SPS_(b > 0)	—	-17.5	—	—	10	45	290	350	—
25	SSRS	—	-17.5	—	—	—	-30	—	—	—
26	UGC_S	-2.5	0	—	—	40	—	—	—	—

*The upper boundary of the Perseus–Pisces ridge as in fig. 4 of Giovanelli, Haynes & Chincarini (1986a).

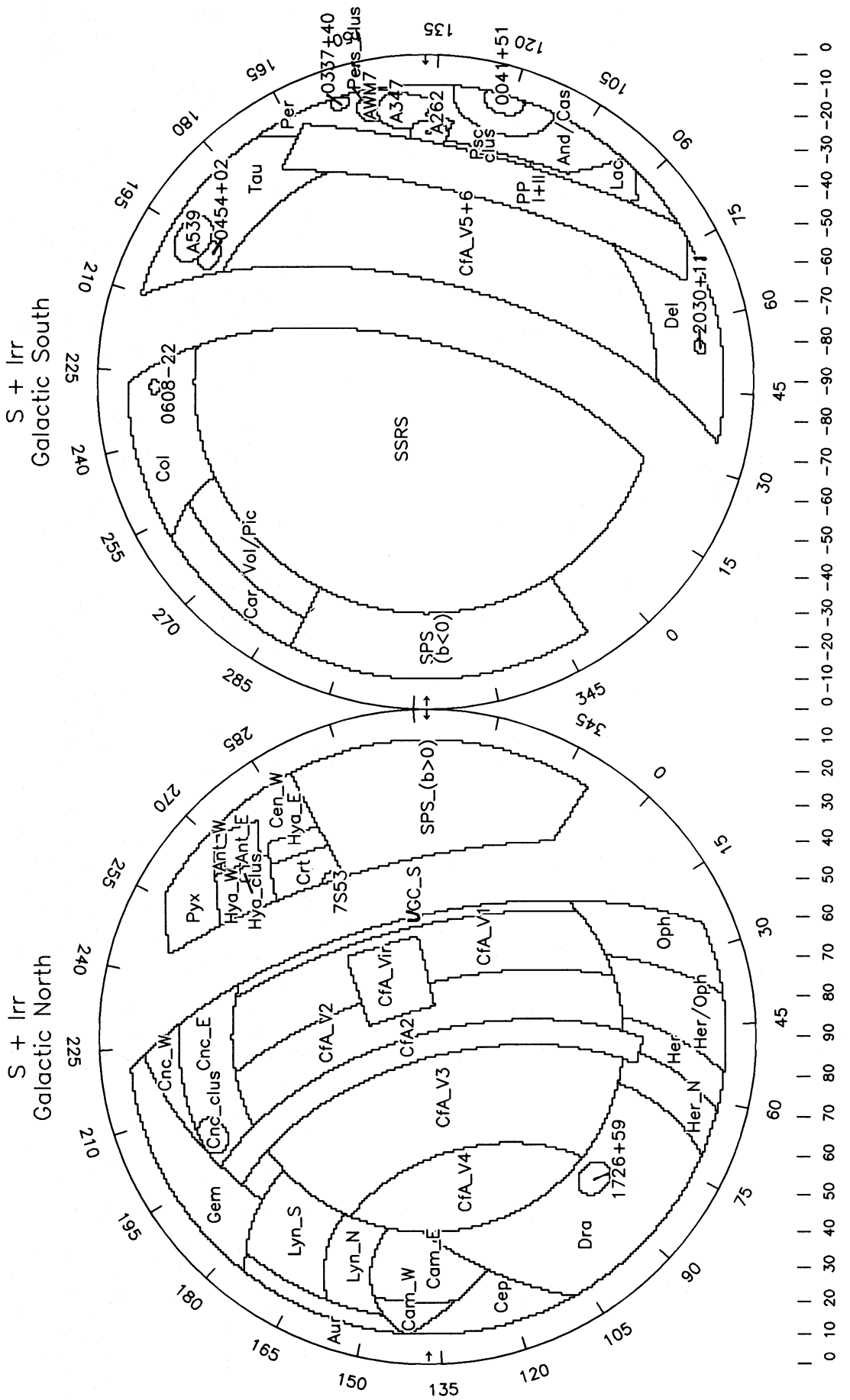

Figure 3. S + Irr zone boundaries.

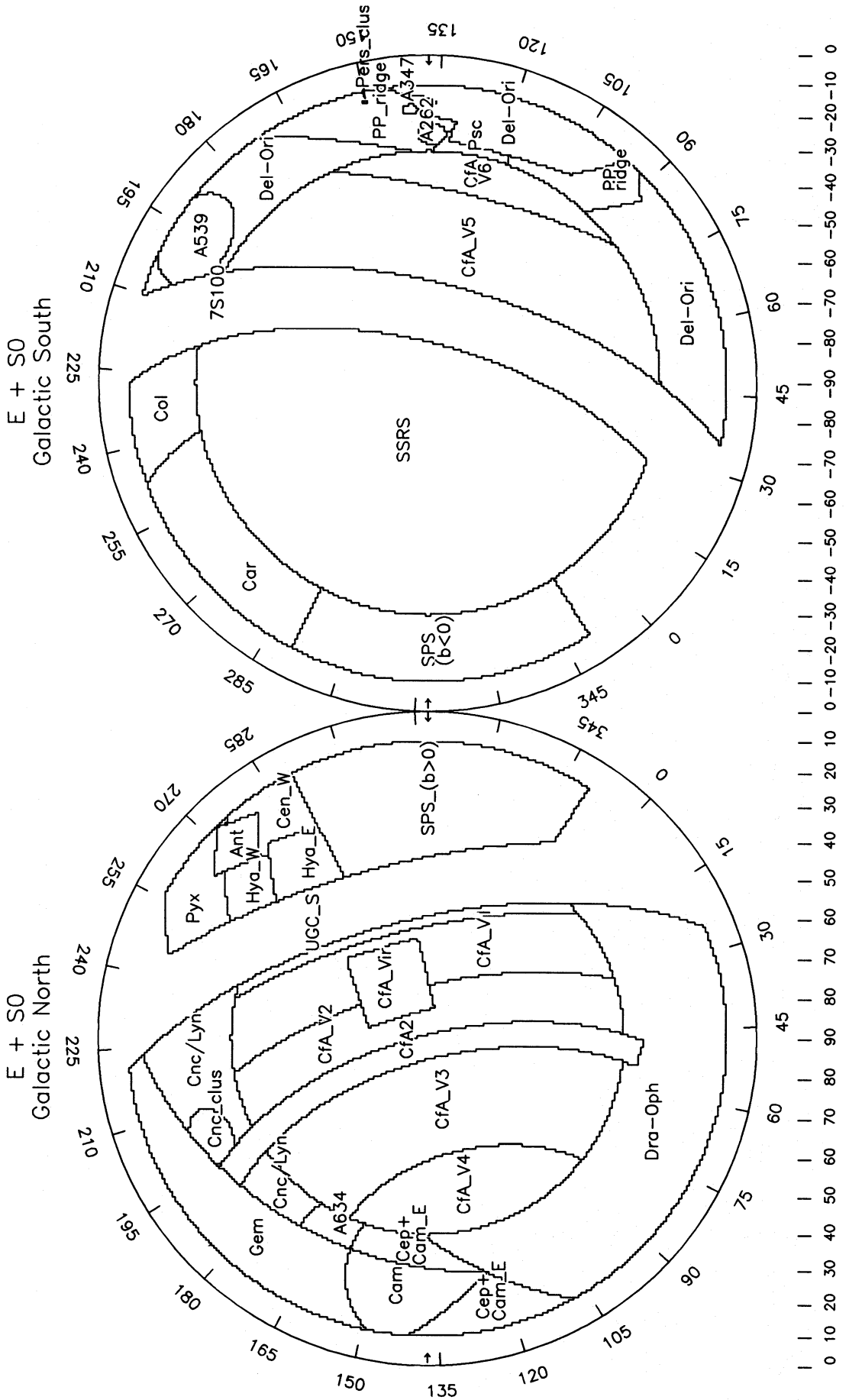

Figure 4. E + S0 zone boundaries.

Table 6. S + Irr field zone completeness.

Zone	Name	N	N_z	$\overline{v_{LG}}$ km s^{-1}	$\overline{\theta}$ arcmin	$\overline{S}$	S_1	S_2	S_3	χ^2
1	And/Cas	83	26	5194.	2.5	0.31	1.14	-3.32	2.73	9.2
2	Ant_E	83	46	2974.	2.6	0.55	1.24	-4.32	5.10	16.2
3	Ant_W	15	11	4355.	2.1	0.73	1.08	-1.48	0.95	2.4
4	Aur	18	15	4555.	1.8	0.83	0.32	3.87	-5.53	0.9
5	Cam_E	216	136	3149.	2.4	0.63	1.03	-0.47	-1.07	17.2
6	Cam_W	46	37	4267.	2.1	0.80	0.85	0.07	-0.50	10.4
7	Car	70	20	2578.	3.1	0.29	1.29	-6.34	7.92	6.9
8	Cen_W	118	43	3623.	3.0	0.36	0.91	-2.64	1.96	4.5
9	Cep	48	24	2967.	2.6	0.50	1.13	-2.40	1.48	7.8
10	CfA1_V1	420	157	3351.	2.9	0.37	1.09	-3.01	2.37	18.3
11	CfA1_V2	388	119	3512.	2.6	0.31	1.06	-2.89	2.20	19.0
12	CfA1_V3	854	309	3005.	3.1	0.36	0.91	-2.15	1.40	5.3
13	CfA1_V4	311	125	2740.	2.8	0.40	0.93	-2.35	1.80	13.4
14	CfA1_V5+6	876	218	4465.	2.4	0.25	0.68	-1.38	0.71	20.5
15	CfA1_Vir	272	142	1574.	3.1	0.52	0.89	-1.64	0.84	18.2
16	CfA2	276	220	5509.	2.0	0.80	0.95	-0.04	-0.68	10.9
17	Cnc_E	131	88	4066.	1.9	0.67	1.06	-1.06	0.26	9.1
18	Cnc_W	34	10	4564.	1.7	0.29	0.68	-1.18	0.64	3.6
19	Col	195	26	3091.	3.8	0.13	0.27	-0.68	0.37	8.4
20	Crt	55	33	4080.	2.9	0.60	1.02	-0.30	-2.74	3.1
21	Del	78	30	4495.	1.9	0.38	1.17	-2.99	2.26	6.9
22	Dra	305	65	3689.	2.5	0.21	1.03	-3.10	2.47	28.6
23	Gem	133	107	4740.	1.7	0.80	1.01	-0.14	-0.57	0.3
24	Her	55	23	4997.	1.9	0.42	1.13	-2.29	1.10	15.5
25	Her/Oph	70	51	4648.	1.7	0.73	1.06	-1.06	0.61	4.3
26	Her_N	54	13	5382.	1.7	0.24	0.49	-0.97	0.82	2.6
27	Hya_E	34	25	4565.	2.9	0.74	1.03	-0.56	-0.77	1.7
28	Hya_W	92	55	3676.	3.0	0.60	0.96	-0.34	-2.28	2.3
29	Lac	50	23	5203.	2.1	0.46	1.12	-2.84	2.52	6.7
30	Lyn_N	100	55	4567.	2.0	0.55	1.09	-1.65	0.68	15.8
31	Lyn_S	124	63	3976.	2.0	0.51	1.10	-1.79	0.81	15.5
32	Oph	43	18	3342.	2.7	0.42	0.84	-1.77	1.21	16.2
33	PP(I+II)	430	393	5840.	1.8	0.91	0.92	0.21	-0.47	2.9
34	Per	100	23	5292.	2.1	0.23	0.50	-0.67	0.02	5.6
35	Pyx	156	32	2068.	3.9	0.21	0.42	-1.31	0.99	6.9
36	SPS_($b < 0$)	364	261	4027.	2.3	0.72	0.84	1.75	-5.58	9.7
37	SPS_($b > 0$)	960	663	4593.	2.3	0.69	0.97	0.52	-3.55	7.6
38	SSRS	2065	1262	5035.	2.6	0.61	0.99	-0.29	-2.29	11.5
39	Tau	76	47	5149.	1.6	0.62	1.10	-1.79	1.43	5.6
40	UGC_S	74	52	3653.	2.3	0.70	1.08	-1.41	0.77	9.4
41	Vol/Pic	98	35	4853.	2.4	0.36	0.94	-3.24	3.81	7.0

Table 7. S + Irr completeness (cluster zones).

Zone	Name	N	N_z	$\overline{v_{LG}}$ km s^{-1}	$\overline{\theta}$ arcmin	$\overline{S}$	S_1	S_2	S_3	χ^2
42	A262_core	9	9	5182.	1.6	1.00	1.00	0.00	0.00	0.0
43	A539	15	15	6337.	1.8	1.00	1.00	0.00	0.00	0.0
44	Cnc_clus	35	34	4948.	1.9	0.97	0.95	0.02	0.05	1.1
45	0041+51_core	12	11	5178.	1.5	0.92	0.66	1.72	-2.15	0.1
46	0337+40	11	10	5491.	1.6	0.91	1.05	-0.83	1.00	1.4
47	0454+02	22	21	6007.	1.6	0.95	0.38	2.49	-2.49	0.6
48	1726+59	35	15	5469.	1.5	0.43	-0.37	4.07	-4.50	0.8
49	0608-22	8	6	1937.	3.2	0.75	1.14	-2.49	2.07	1.1
50	A262_halo	37	24	5068.	1.9	0.65	1.01	-1.44	1.07	12.1
51	A347	98	47	4735.	2.5	0.48	1.15	-2.78	2.04	20.0
52	Per_clus	5	5	4928.	1.3	1.00	1.00	0.00	0.00	0.0
53	Hya_clus	22	19	3614.	2.5	0.86	0.73	2.70	-6.75	0.3
54	AWM7	40	17	4563.	2.1	0.43	1.16	-2.90	2.23	4.8
55	0041+51_halo	47	25	4900.	1.9	0.53	0.72	0.66	-2.14	6.1
56	2030+11	5	5	4802.	2.1	1.00	1.00	0.00	0.00	0.0
57	7S053	13	12	2240.	4.4	0.92	1.03	-0.59	0.11	0.9

Table 8. E + S0 completeness.

Zone	Name	N	N_z	$\overline{v_{LG}}$ km s^{-1}	$\overline{\theta}$ arcmin	$\overline{S}$	S_1	S_2	S_3	χ^2
				Field Zones						
1	Ant	22	19	3954.	2.2	0.86	0.83	1.65	-3.96	0.0
2	Cam	28	8	4527.	1.8	0.29	1.09	-3.77	3.89	5.2
3	Car	33	13	4177.	2.0	0.39	0.09	3.39	-6.48	1.7
4	Cen_W	16	12	2966.	2.8	0.75	0.70	2.51	-6.89	1.9
5	Cep+Cam_E	15	9	3659.	2.0	0.60	0.48	1.46	-2.76	1.5
6	CfA1_V1	76	58	3638.	2.2	0.76	1.06	-1.15	0.73	5.5
7	CfA1_V2	82	53	5036.	1.8	0.65	1.10	-1.74	1.39	6.7
8	CfA1_V3	104	77	4383.	2.1	0.74	1.00	0.01	-1.23	6.3
9	CfA1_V4	49	41	3203.	2.4	0.84	0.98	0.28	-1.25	0.9
10	CfA1_V5	194	88	4811.	2.0	0.45	1.10	-1.87	0.72	6.5
11	CfA1_V6	67	38	5439.	1.8	0.57	1.02	-0.43	-1.08	2.4
12	CfA1_Vir	99	87	1531.	2.9	0.88	1.01	-1.10	1.42	12.3
13	CfA2	57	55	6267.	1.8	0.96	0.93	0.47	-0.75	0.7
14	Cnc/Lyn	24	7	4871.	1.6	0.29	1.18	-3.24	2.61	5.5
15	Col	39	8	6285.	2.6	0.21	0.24	0.15	-0.74	2.0
16	Del-Ori	54	4	4249.	2.2	0.07	0.37	-1.02	0.70	2.9
17	Dra-Oph	73	21	5039.	1.9	0.29	1.15	-2.78	1.74	8.5
18	Gem	35	26	5722.	1.6	0.74	1.02	-0.41	-0.39	3.3
19	Hya_E	15	15	3020.	2.4	1.00	1.00	0.00	0.00	0.0
20	Hya_W	32	31	3733.	1.9	0.97	1.00	0.09	-0.40	1.2
21	PP_ridge	124	29	5572.	2.3	0.23	0.48	-1.09	0.87	15.7
22	Pyx	38	13	3213.	2.9	0.34	0.89	-2.23	1.11	4.9
23	SPS_($b < 0$)	50	39	3846.	2.1	0.78	0.85	1.65	-4.61	1.1
24	SPS_($b > 0$)	255	219	4384.	2.3	0.86	0.87	1.45	-3.93	3.2
25	SSRS	402	326	5641.	2.1	0.81	0.87	1.40	-4.11	4.3
26	UGC_S	6	5	6420.	1.6	0.83	1.03	-0.54	0.25	0.9
				Cluster Zones						
27	A262	14	12	5184.	1.7	0.86	0.74	1.62	-2.50	0.1
28	A347	7	7	6004.	1.8	1.00	1.00	0.00	0.00	0.0
29	Pers_clus	8	8	5140.	1.8	1.00	1.00	0.00	0.00	0.0
30	A539	6	6	4933.	1.5	1.00	1.00	0.00	0.00	0.0
31	Psc_clus	16	10	5244.	1.9	0.63	1.11	-1.97	1.57	2.5
32	Cnc_clus	6	6	3852.	1.6	1.00	1.00	0.00	0.00	0.0
33	A634	7	6	4327.	1.8	0.86	0.89	0.86	-1.66	0.0
34	7S100	2	2	3746.	2.0	1.00	1.00	0.00	0.00	0.0

the mean density or 0.4 of a contour, so only differences greater than 1 contour are significant. The agreement between the two maps is good.

In summary, we conclude that the adopted zone boundaries and completeness functions adequately characterize the completeness of the redshift subsample.

5 RECONSTRUCTING THE DENSITY FIELD

Having determined the completeness of the redshift sample, we now describe our method for determining the smoothed density field, which is similar to the method of weights of Yahil et al. (1980; see also Lynden-Bell & Lahav 1988). The idea is to assign extra weight to each galaxy in the redshift sample to compensate for those galaxies in the underlying density field that were not selected. To calculate the weights it is necessary to know the redshift completeness, which was determined in the preceding section, and the distribution of metric diameters, the diameter function $\phi(D)$. The diameter function was investigated in HL-B and is discussed in Section 5.1. The adopted weighting scheme is discussed in Section 5.2. In calculating the weights and diameter functions, we have semi-volume-limited the sample at $D_{\rm min} = 1500$ km s^{-1} arcmin, and we continue to treat E + S0 and S + Irr galaxies separately. The weighted galaxies are then smoothed to produce a density field. However, we wish to know the density field, not in pseudo-3D redshift space, but in distance space. Assuming that mass is related to light and adopting a value of Ω, we can use the optical density field to predict peculiar velocities at any position using linear theory. An iterative method, similar to that of YSDH, is used to transform self-consistently from redshift space to distance space: at each iteration, the peculiar velocity is calculated at the current position of each galaxy; this is then subtracted from the galaxy's redshift to update its distance for the next iteration. This procedure is described in more detail in Section 5.6.

5.1 Diameter functions

For the diameter function, $\phi(D)$, we adopt the functional form given by equation (6) of HL-B, which has one free

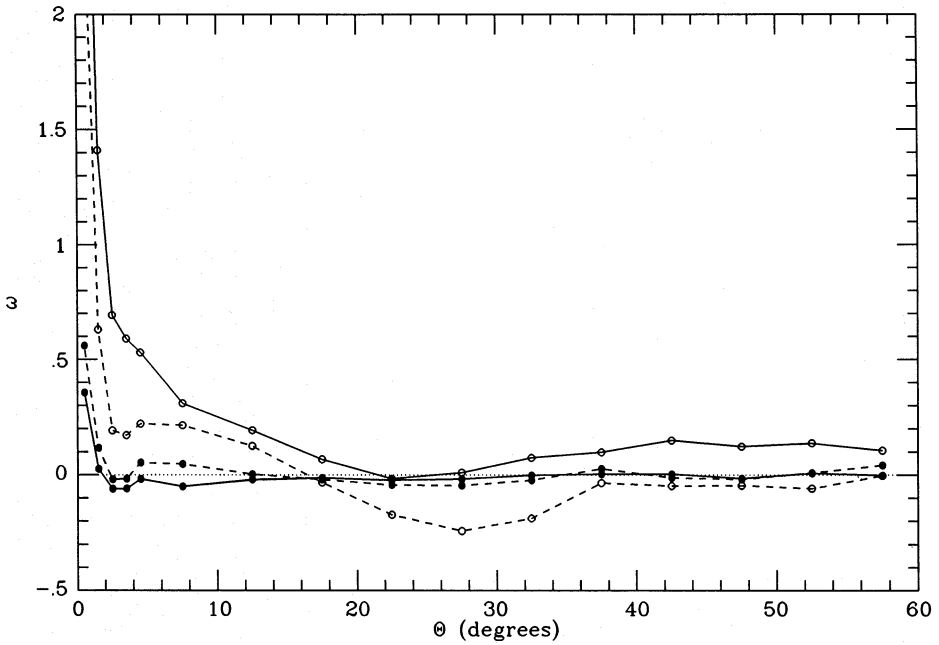

Figure 5. Angular correlation functions for the redshift subsample. The excess correlation of the redshift subsample relative to the U+E catalogue is indicated by the filled circles, and the autocorrelation of the redshift subsample is indicated by open circles. Both functions are evaluated only in the unsurveyed area. Solid lines connect the symbols for the UGC unsurveyed area, whereas dashed lines connect the symbols for the ESO unsurveyed area.

parameter: a characteristic metric diameter, D_L. The UGC diameter functions are determined from the CfA1 zones (excluding the Virgo zone) and the CfA2 zone, allowing for the different completeness in each zone. The ESO diameter functions are calculated using the single SSRS zone.

Whereas HL-B used simple Virgo infall models, here we recalculate the diameter functions at each iteration, using the current distances from the iterative method described in Section 5.6 below. The diameter functions typically converge within three iterations. We continue to treat S+Irr and E+S0 galaxies separately, and obtain a final D_L (errors from the SSRS determination) of 4290 ± 130 km s^{-1} arcmin $=12.4\pm0.4$ h^{-1} kpc for S+Irr galaxies and 4380 ± 290 km s^{-1} arcmin $=12.7\pm0.8$ h^{-1} kpc for E+S0 galaxies, after scaling ESO diameters to the 25 B mag arcsec^{-2} isophote using the linear transformation of RC3. We then scale UGC diameters by a factor so that their scaled diameter functions match the scaled ESO diameter functions. ESO is deeper than UGC, and the ratio of diameter scales (average over all types) of 1.16 ± 0.05 found here is comparable to the ratio found by HL-B (1.13–1.19 depending on Virgo infall) and is somewhat larger than the ratio of 1.10 one obtains from the UGC and ESO major diameter transformations given in RC3.

5.2 Weighting schemes

Knowing the diameter function and completeness, we can calculate the selection function (the probability that a galaxy is included in the redshift subsample) at any position. To weight galaxies *by number* we just assign a weight equal to the inverse of the selection function to each galaxy in the redshift subsample (HL-B),

$$w_n(r,\hat{\boldsymbol{r}})=\frac{\int_{D_{\min}}^{\infty}\phi(D)\,\mathrm{d}D}{\int_{D_0(r)}^{\infty}\phi_z(D,r,\hat{\boldsymbol{r}})\,\mathrm{d}D}, \tag{6}$$

where the 'selected' distribution of metric diameters is $\phi_z(D,r,\hat{\boldsymbol{r}})\equiv C(D/r,\hat{\boldsymbol{r}})S(D/r,\hat{\boldsymbol{r}})\phi(D)$ and the lower limit on the integral is $D_0(r)=\max(D_{\min},r\theta_0)$. We have also examined a number of other selection effects that may bias the weighting scheme. For example, a sharp magnitude limit becomes a 'fuzzy' cut-off in diameter. Once the selection by diameter has been taken into account, however, the remaining biases are smaller than e.g. random errors in the diameter function parameter D_L (Hudson 1992). Similarly, biases introduced by velocity limits (e.g. redshift surveys from a radio telescope) are negligible for the redshift sample used here (Hudson 1992).

Note that the method of weights simply assigns extra weight to those galaxies with redshifts to compensate for the galaxies in the same volume element that do not have measured redshifts. This is equivalent to placing the unobserved galaxies at the position of the galaxy with redshift. One might object that we are throwing away some detailed information about the galaxies without redshifts, namely their positions on the sky. Except on small scales, however, most of this information has already been processed in determining the completeness functions, which in turn are absorbed into $w_n(r,\hat{\boldsymbol{r}})$. The distance of a galaxy without a measured redshift can be determined only from its angular diameter, which is a poor estimator of distance. Thus, if we attempted to use these galaxies at this stage, we would obtain only a marginally improved estimate of the density field at the cost of drastically complicating our procedure. Furthermore, as we will be smoothing the density field over 500 km s^{-1} scales, which is of the order of the interparticle spacing of

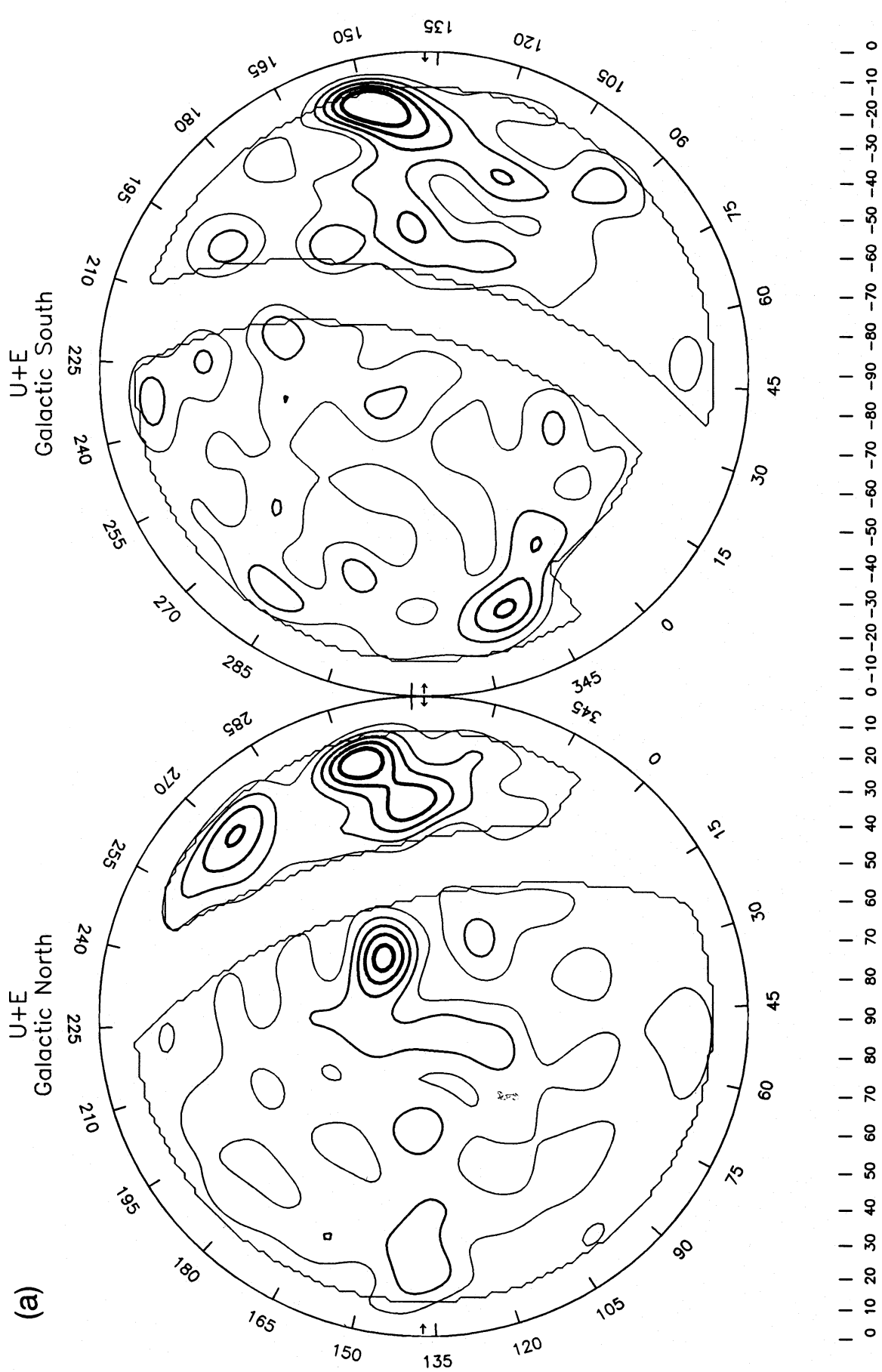

Figure 6. The surface number density of galaxies on the sky is shown. The surface density has been constructed using all spherical harmonic coefficients with $l \leq 20$ (see text for details). The effective smoothing scale is $\sim 9°$. The first contour is at the mean surface density and subsequent contours are multiples of the mean density. There is no interpolation into the masked area (indicated by the jagged line); consequently the density there is approximately zero. Note the strong double peak in Centaurus ($l \approx 310°$, $b \approx 20°$ and $l \approx 330°$, $b \approx 30°$) and at Perseus ($l \approx 150°$, $b \approx -15°$). (a) All galaxies in U + E with $|b| > 12°$ are used. (b) Only galaxies in the redshift subsample, weighted by $1/S(\theta, \hat{r})$, are used. The noise level of the weighted redshift map is about 0.4 times the mean density, so only differences greater than 1 contour are significant. The good agreement between the two maps indicates that our mapping of the redshift completeness on these scales is good.

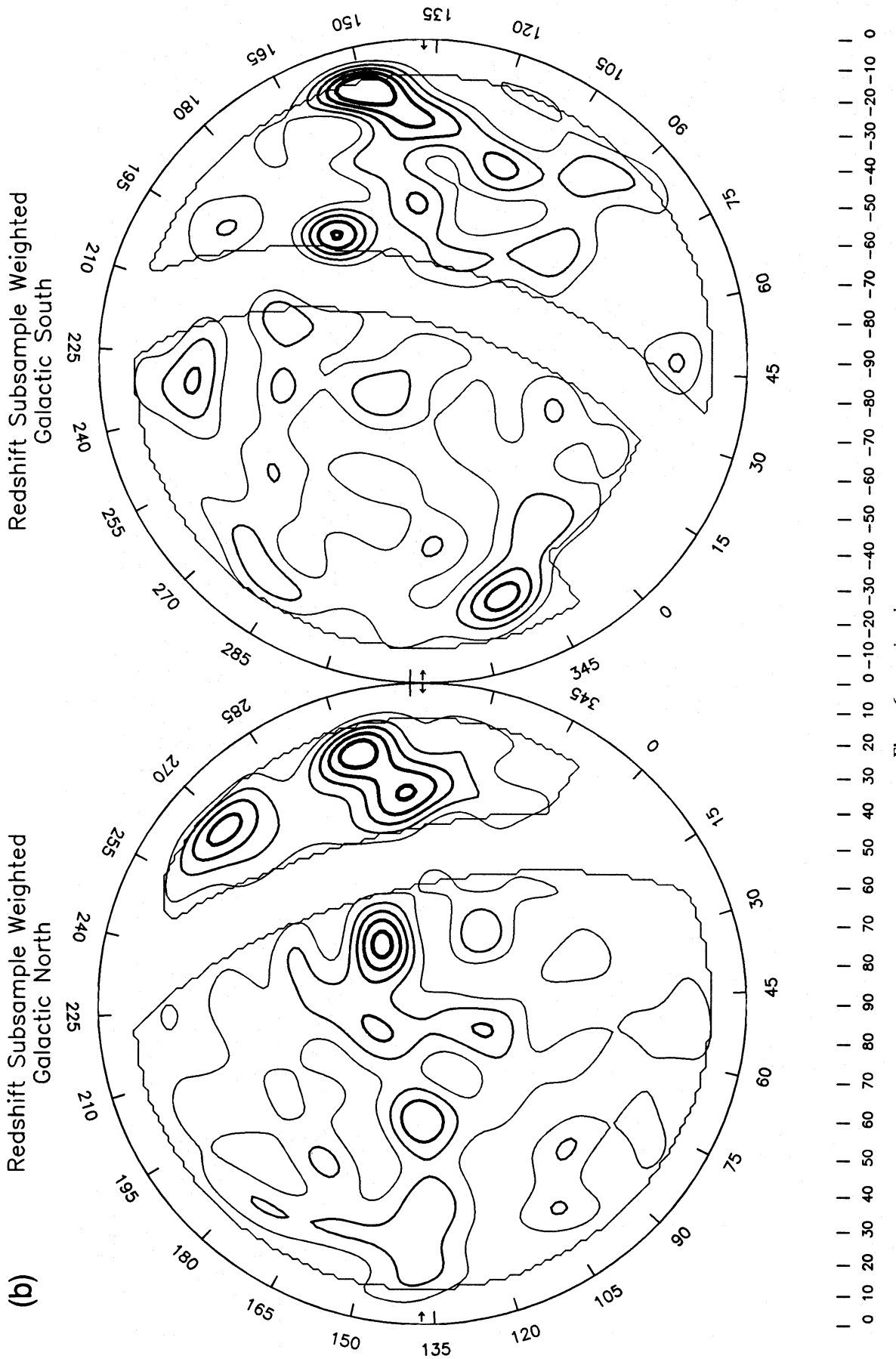

Figure 6 – *continued*

the weighted galaxies, the details of the density field on scales smaller than 500 km s^{-1} are largely irrelevant.

It is reasonable to assume that the total mass of a galaxy halo is correlated with the galaxy's luminosity. Rather than use the simple number weighting scheme, we therefore prefer to incorporate this assumption into the weighting scheme. Because we do not know the luminosities of most of the galaxies in the sample, we shall assume that the square of a galaxy's metric major diameter, D^2, is a good estimator of luminosity and hence of mass. In fact, diameter–linewidth relations, similar to the Tully–Fisher luminosity–linewidth relation, have been investigated by a number of authors (Tully & Fisher 1977; Cornell et al. 1987; Staveley-Smith & Davies 1989). The existence of such a relationship (albeit with greater scatter than the luminosity–linewidth relation) provides evidence that diameter is correlated with mass in the luminous parts of spiral galaxies. Henceforth, we use the term 'luminosity' as a shorthand for D^2. We now introduce a weighting scheme which considers the 'luminosity' of the galaxy in the redshift sample and the 'luminosity' of the unobserved galaxies. This weighting function, w_L, adds the expected amount of unobserved 'luminosity' to the observed 'luminosity':

$$w_L(D, r, \hat{\boldsymbol{r}}) = D^2 + \tilde{D}^2(r, \hat{\boldsymbol{r}}), \tag{7}$$

where

$$\tilde{D}^2(r, \hat{\boldsymbol{r}}) = \left(\frac{\int_{D_{\min}}^{\infty} D^2 \phi(D)\, \mathrm{d}D - \int_{D_0(r)}^{\infty} D^2 \phi_z(D, r, \hat{\boldsymbol{r}})\, \mathrm{d}D}{\int_{D_0(r)}^{\infty} \phi_z(D, r, \hat{\boldsymbol{r}})\, \mathrm{d}D} \right). \tag{8}$$

An analogous expression was used by Moore, Frenk & White (1993) for luminosity weighting. If we calculate the expectation value of this weight over the distribution of metric diameters of galaxies with measured redshifts, at fixed r, we find that

$$\langle w_L \rangle = \langle D^2 \rangle w_n, \tag{9}$$

where

$$\langle D^2 \rangle = \frac{\int_{D_{\min}}^{\infty} D^2 \phi(D)\, \mathrm{d}D}{\int_{D_{\min}}^{\infty} \phi(D)\, \mathrm{d}D} \tag{10}$$

is just the average 'luminosity' per galaxy. As r goes to zero, w_L reduces to D^2 as desired, but at large distances $\tilde{D}^2(r, \hat{\boldsymbol{r}})$ dominates and the weighting is proportional to the number weighting. At $r = 8000$ km s^{-1}, typical values of w_L are $\approx 90\langle D^2 \rangle$ and do not exceed $\approx 250\langle D^2 \rangle$. Such weights are consistent with those of poor clusters.

In practice, if corrections are made to a galaxy's diameter (e.g. for absorption), the formulae given above are used, except that r is replaced by $r^* \equiv (\theta_c/\theta) r$, where θ_c is the corrected diameter described in Section 2.2.

On large scales, the rms difference between the number-weighted and the 'luminosity'-weighted density fields is much smaller than the shot-noise error in either. Nearby, however, the 'luminosity' weight should be a more accurate indicator of mass, and so we adopt this scheme throughout.

5.3 Models of the density field

We have no data in the masked area, i.e. in the 'missing equatorial strip' between the catalogues ($-17.^\circ5 <$ Dec. $< -2.^\circ5$), in the zone of avoidance, and in the two small regions described in Section 2. Two simple schemes for describing the density field in this area are described below.

In the first model, which we refer to as the 'average mask' model, the masked area is randomly populated with simulated 'galaxies' of identical weight such that the density there is equal to the average density computed from the catalogued areas. The result of this scheme is that the peculiar gravity from the masked area vanishes everywhere. (By contrast, were we to leave this area *empty* it would have a repulsive effect.)

It is not, however, implausible that some superclusters extend into or across the plane or equatorial strip. Such large-scale structures in the masked area are important because they affect the predicted peculiar velocities of all galaxies. The 'cloned mask' model attempts a crude but simple interpolation, by 'cloning' the weighted galaxies in strips adjacent to the zone of avoidance and missing equatorial strip and copying them into the masked areas (cf. Lynden-Bell et al. 1989). For the zone of avoidance, $|b| \le b_{\min}$, we begin with the strip just north of the $b_{\min}$ bounded by $\sin(b_{\min}) < \sin(b) < 2\sin(b_{\min})$. All weighted galaxies within this strip are copied into the region immediately below into the northern galactic half of the zone of avoidance by setting $\sin(b_{\mathrm{new}}) = \sin(b) - \sin(b_{\min})$. Similarly, a strip south of the zone of avoidance is 'cloned' upwards into the southern galactic half of the zone of avoidance. An analogous procedure is carried out for two strips north and south of the missing equatorial strip, where we shift sin(Dec.) rather than sin(b). The galactic longitude or right ascension of the cloning strips is limited so that there is no overlap between the strips to be cloned (so that no galaxy is counted four times) and so that these do not extend into the masked area (e.g. the cloning strip for the zone of avoidance does not extend into the missing equatorial strip). While this exact duplication of the density field is unrealistic on small scales, the small-scale detail of the density field in the masked area is unimportant because we will not be predicting the peculiar velocities of any galaxies within these areas.

At latitudes $b_{\min} = 10^\circ$, the *maximum* correction to diameters is a factor of 1.83, whereas at $b_{\min} = 12^\circ$ this has fallen to a factor of 1.56. We therefore adopt $b_{\min} = 12^\circ$ as the zone of avoidance for the remainder of this work. The zone of avoidance cloning strips are therefore limited to $53^\circ < l < 192^\circ$ and $263^\circ < l < 350^\circ$; the equatorial cloning strips are limited to $20^{\mathrm{h}}28^{\mathrm{m}} < \mathrm{RA} < 4^{\mathrm{h}}44^{\mathrm{m}}$ and $10^{\mathrm{h}}08^{\mathrm{m}} < \mathrm{RA} < 15^{\mathrm{h}}36^{\mathrm{m}}$. The remaining masked area, consisting of two cross-shaped caps where the Galactic Plane and equatorial strip cross, near the Galactic Centre and near $l \approx 240^\circ$, is filled with 'galaxies' with randomly chosen positions as in the average mask model. In summary, regions with data cover 67 per cent of the sky. In the average mask model, the remaining 33 per cent have the average density. In the cloud mask model, 19 per cent of the sky is filled with interpolated densities from adjacent areas, and the remaining 14 per cent have the average density.

Within $r < 8000$ km s^{-1}, we expect a reasonable estimate of the density field, with an error in the mean density of $\simeq 9$ per cent (see Section 6 below). We therefore adopt $r_{\max} = 8000$ km s^{-1} as the distance limit for both the cloned and average mask models, and set the density at $r > r_{\max}$ equal to the average density.

Finally, we assign a 'luminosity' to the Local Group at $r=0$ using the isophotal diameters of the Galaxy and M31: 23 kpc from de Vaucouleurs & Pence (1978); and 38.8 kpc for M31, using θ_{25} from RC2 and assuming a distance of 725 kpc (van den Bergh 1989). We assume $H_0=75$ km s^{-1} Mpc^{-1} to convert their metric diameters to units of km s^{-1} arcmin.

5.4 Collapsing the 'Fingers of God'

A problem arises with clusters of galaxies with large velocity dispersion, the so-called 'Fingers of God' which point towards the origin in redshift plots. In these cases, the velocities of individual galaxies with respect to the centre of mass of the cluster carry no information about their initial conditions. We therefore wish to collapse the 'Fingers of God' by replacing the velocity of each galaxy in a cluster with the cluster median.

To identify clusters we use a percolation or 'friends-of-friends' algorithm described in Huchra & Geller (1982). We scale the linking lengths according to the prescription of Moore et al. (1993), except that we use the selection function $w_n^{-1}(r,\hat{r})$ in place of their luminosity-based selection function. In the direction perpendicular to the line of sight, we adopt a transverse linking length (D_0 in their equation 2) of 53 km s^{-1}, so that the minimum overdensity is 30 at a fiducial velocity of 1250 km s^{-1}. Along the line of sight, we adopt a velocity linking length (V_0 in their equation 3) of 750 km s^{-1} because this value predicts the correct abundance of high velocity dispersion objects in comparison with CDM N-body simulations (Moore et al. 1993). We find, however, that the algorithm fails near the origin and adds some galaxies to Virgo and Ursa Major that are part of the nearer Coma–Sculptor Cloud. We therefore remove 'by hand' the nearby (large angular diameter) galaxies that would otherwise bias the 'luminosity' of these clusters if they were placed at the distance of the cluster.

The groups compare well with those found by 7S, but the match is not strictly one-to-one. In a future paper, we will compare our results with the 7S distances. We therefore merge our groups to match theirs where necessary. The percolation algorithm also merges the 7S groups 35, 58 (Cen 30) and 59 (Cen 45) into one group and the 7S groups 55 and 235 into another. In addition, we find 31 groups that are not identified with 7S groups. For the final list we select every group that is identified with a 7S group or a known cluster, and other groups with more than 10 members. We are left with 135 rich groups/clusters. For each of these we replace the individual galaxy redshifts with the group median redshift. This procedure has the advantage that it mitigates the evacuation of the 'triple-valued regions', as described in more detail in Section 5.6 below. The Virgo cluster has the most members (149) and a median heliocentric velocity of 1156 km s^{-1} (1070 km s^{-1} in the Local Group frame).

5.5 Peculiar velocities from the smoothed density field

At this stage, the density field is described by a set of weighted points. In linear theory, the peculiar velocities are proportional to the acceleration and are given by

$$\boldsymbol{u}(\boldsymbol{r})=\frac{f(\Omega)}{4\pi}\int \delta(\boldsymbol{r}')\frac{\boldsymbol{r}'-\boldsymbol{r}}{|\boldsymbol{r}'-\boldsymbol{r}|^3}\,\mathrm{d}^3\boldsymbol{r}' \tag{11}$$

(Peebles 1980), where $f(\Omega)\simeq\Omega^{0.6}$ and $\delta(\boldsymbol{r})=[\rho(\boldsymbol{r})-\overline{\rho}]/\overline{\rho}$ are the fluctuations in *mass* density about the mean. Note that this expression is independent of the Hubble constant because we express distances, r, in units of km s^{-1}. We shall assume that mass is related to light by the prescription of linear biasing

$$\delta_{\mathrm{L}}(\boldsymbol{r})=b_{\mathrm{o}}\delta(\boldsymbol{r}), \tag{12}$$

where b_{o} is the biasing parameter for the 'luminosity'-weighted density field of optical galaxies. We thus replace $f(\Omega)$ by $\beta_{\mathrm{o}}\equiv f(\Omega)/b_{\mathrm{o}}$ when we use $\delta_{\mathrm{L}}(\boldsymbol{r})$ in place of $\delta(\boldsymbol{r})$ in equation (11). Note that, in linear theory, this is equivalent to having a fraction $1/b_{\mathrm{o}}$ of the global mean mass density, Ω, clustered with the observed galaxies, and distributing the remainder in a uniform component.

At this stage, the optical density field is a set of weighted delta functions. It is necessary to smooth these to obtain a density field for which linear theory is appropriate. Using N-body experiments and simulating their *IRAS* 2-Jy sample, Davis, Strauss & Yahil (1991) found that with 500 km s^{-1} radius top-hat smoothing, linear theory was a good approximation to the true peculiar velocities, accounting for all but 1/6 of the kinetic energy. Smoothing the density field with a top-hat is equivalent to smoothing the force with the window function

$$W_{\mathrm{s}}(|\boldsymbol{r}'-\boldsymbol{r}|)=\begin{cases}\dfrac{|\boldsymbol{r}'-\boldsymbol{r}|^3}{r_{\mathrm{s}}^3} & |\boldsymbol{r}'-\boldsymbol{r}|<r_{\mathrm{s}},\\ 1 & |\boldsymbol{r}'-\boldsymbol{r}|\geq r_{\mathrm{s}}.\end{cases} \tag{13}$$

Within a typical 500 km s^{-1} radius sphere, we expect ≈ 20 galaxies with redshifts nearby; ≈ 1 galaxy at 6000 km s^{-1}; and ≈ 0.3 galaxies at 8000 km s^{-1}. For simplicity, we therefore adopt $r_{\mathrm{s}}=500$ km s^{-1}, independent of distance.

Rather than calculate the acceleration from a smoothed field via Fourier methods, we calculate it directly by summing over all weighted particles. The predicted peculiar velocity of a galaxy with respect to the frame defined by the optical density field is given by

$$\boldsymbol{u}_{\mathrm{o}}(\boldsymbol{r})=\beta_{\mathrm{o}}\left(\frac{1}{4\pi\overline{\rho}_{\mathrm{L}}}\left[\sum_i W_{\mathrm{s}}(|\boldsymbol{r}_i'-\boldsymbol{r}|)\,w_{\mathrm{L}}(D_i,\boldsymbol{r}_i')\frac{\boldsymbol{r}_i'-\boldsymbol{r}}{|\boldsymbol{r}_i'-\boldsymbol{r}|^3}\right]+\frac{\boldsymbol{r}}{3}\right), \tag{14}$$

where $\overline{\rho}_{\mathrm{L}}$ is the average D^2 density. The last term on the right-hand side of equation (14) gives the contribution of an average-density universe; this is needed because the summation calculates the contribution from the density rather than the overdensity.

We have one remaining parameter to fix: β_{o}, which scales the peculiar velocities in equation (14). For the average mask model, we iterate from redshift to distance space by fixing $\beta_{\mathrm{o}}=0.5$, whereas for the cloned mask model we iterate using $\beta_{\mathrm{o}}=0.4$. These values give the best fit to the observed peculiar velocities (Hudson 1992; see also Section 9 below), although all results do not differ significantly if β_{o} is varied by ± 0.1.

5.6 Iterative transformation from redshift to distance space

Given a smoothed density field, the peculiar velocity at any arbitrary position can be calculated using linear theory. The problem is that, a priori, we do not know the galaxy distances, r, only their measured redshift velocities, $v_{LG} = cz_{LG}$. To translate from redshift space to distance space, we adopt an iterative scheme (cf. YSDH) as follows.

(1) Make an initial estimate of the distance of every galaxy in the redshift subsample. A good estimate of the galaxy's distance will speed up the convergence of the iterative procedure. The $D_n - \sigma$ distance of the appropriate 7S group is used as the initial distance of galaxies in groups. For galaxies not in groups, and for groups not identified with a 7S group, we fix their initial distance using the Virgo plus Great Attractor infall model of FB88. We stress that these distance estimates are only used as *initial* distances in the iterative procedure – the final distances are determined self-consistently from the optical density field and the resulting peculiar velocity field as described below. (We have verified that, if galaxy distances are initialized to their velocity in the Local Group frame, the resulting density field is the same.)

(2) Calculate the diameter functions as described in Section 5.1, using the current distances.

(3) Calculate the weights of each galaxy using equation (7) at their current distances. In the average mask model, the positions of the random 'galaxies' are fixed. For the cloned mask model, we perform the 'cloning' at each iteration using the current weights and distances of galaxies in the cloning strips. To truncate the density field at $r = r_{max}$, we set the weights of galaxies with $r > r_{max} + r_s$ to zero. This smoothing scheme treats galaxies as spheres of radius r_s with total 'luminosity' w_L. Therefore, when a galaxy lies within the shell $|r - r_{max}| < r_s$, we calculate how much of its sphere lies within r_{max} and adjust its weight accordingly.

(4) Calculate the peculiar velocity of each galaxy at its current distance plus that of the Local Group (at $r = 0$) using equation (14). The distance of each galaxy is then updated by setting

$$r \leftarrow v_{LG} - [\boldsymbol{u}_o(\boldsymbol{r}) - \boldsymbol{u}_o(0)] \cdot \hat{\boldsymbol{r}}, \tag{15}$$

where the term in square brackets is the predicted peculiar velocity in the Local Group frame. In practice, we find that the distances of some galaxies oscillate from one solution to another at alternate iterations. This usually occurs in triple-valued regions (see below). Following YSDH, at each iteration we set the peculiar velocity of a galaxy to the average of its peculiar velocity at its current position as calculated above and its peculiar velocity from the previous iteration. While this slows down the convergence, it damps our oscillations in situations where the peculiar velocities might otherwise bounce from one solution to another.

(5) If we have performed less than eight iterations, loop back to step 2.

This iterative procedure is stopped after eight iterations. The difference between peculiar velocities on the eighth and seventh iterations is plotted against the peculiar velocities on the eighth iteration for all galaxies in Fig. 7. Most galaxies converge to within 10 km s^{-1} and over 99 per cent converge to within 50 km s^{-1}.

In regions of high density, such as around clusters, it can be the case that along a given line of sight there are three values of r at which the same v is predicted (the so-called 'triple-valued regions'). The simple method described above will always place the galaxy at one of the two outer solutions of $v(r) = u_o(r) + r$, and never at the middle solution. However, this effect is mitigated by the percolation procedure of

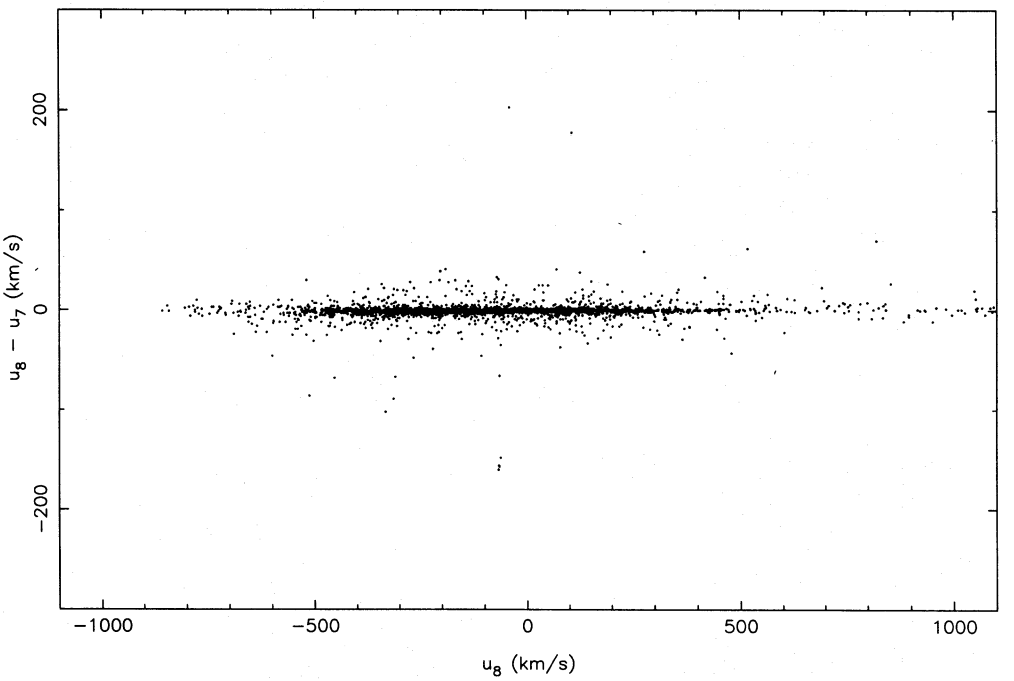

Figure 7. Convergence of the iterative method. The difference in the peculiar velocities on the eighth and seventh iterations is plotted against the peculiar velocity on the eighth iteration for all galaxies. Most peculiar velocities have converged to within 30 km s^{-1}.

Section 5.4, which places some galaxies at the cluster centre, close to the middle solution. (See also YSDH, who describe two alternative, but somewhat more complicated, schemes for dealing with triple-valued regions.)

6 THE DENSITY FIELD

Fig. 8 shows the density field of the cloned mask model within 2000 km s^{-1}. The left-hand panels show all weighted galaxies within 500 km s^{-1} of the Supergalactic Plane. The top panels are in redshift space, and the bottom panels show the results after the collapse of the 'Fingers of God' and the iteration to distance space. Note the cloning of structures into the zone of avoidance and into the missing equatorial strip, and the evacuation of the triple-valued regions. The right-hand panels show the density field smoothed with a 500 km s^{-1} Gaussian, i.e. with the filter

$$W_G(r) \propto \exp\left(-\frac{r^2}{2r_G^2}\right), \tag{16}$$

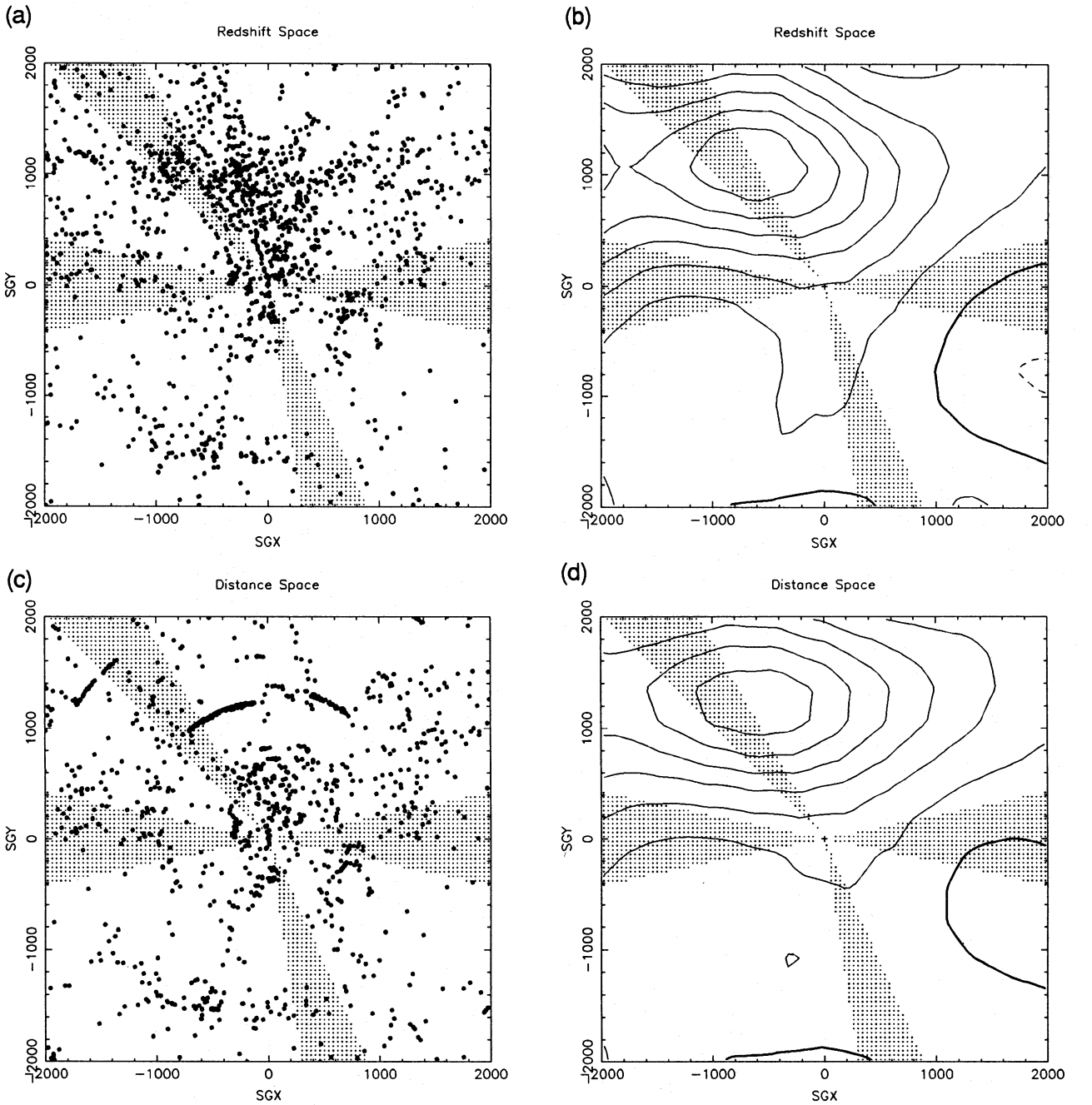

Figure 8. The Supergalactic Plane. The masked area is shaded. (a) All weighted galaxies within 500 km s^{-1} of the Supergalactic Plane are shown, in redshift space. Note the 'cloning' of structures into the zone of avoidance and into the missing equatorial strip. (b) The density field in redshift space after smoothing with a 500 km s^{-1} Gaussian filter. The heavy contour indicates the mean density and the contour spacing is $\Delta\delta = 0.5$. (c) As (a), but after the collapse of the 'Fingers of God' and the iteration to distance space. Note the evacuation of the triple-valued zones around the Virgo and Ursa Major clusters. Also note that, within the collapsed part of these clusters, many of the plotted points overlap. (d) As (b), but after iteration to distance space.

where $r_G = 500$ km s^{-1}. (This smoothed density field is similar to the one from which we calculate the peculiar velocities.) Note that nearby there is little difference between redshift space and distance space, although the Virgo supercluster's centre and amplitude do change slightly. The transformation from redshift space is more important for more distant galaxies, because the weighting function increases rapidly with distance (see Kaiser 1987; Kaiser & Lahav 1988).

The density in a given volume is obtained by summing over all weights within the volume V:

$$\rho_L(V) = \frac{1}{V} \sum_{i \in V} w_L(\boldsymbol{r}_i). \tag{17}$$

The shot-noise error in $\rho_L(V)$ is simply

$$\Delta\rho_L(V) = \frac{1}{V}\left[\sum_{i \in V} w_L^2(\boldsymbol{r}_i)\right]^{0.5}. \tag{18}$$

We can then easily obtain $\delta_L(V) = [\rho_L(V) - \overline{\rho}_L]/\overline{\rho}_L$ for all types, or for E + S0 and S + Irr galaxies separately.

We compute the mean density, $\overline{\rho}_L$, by summing over the whole sky to a distance $r_{max} = 8000$ km s^{-1}. For the average mask model, the mean 'luminosity' (D_{25}^2) density is 1.07 (km s^{-1} arcmin)^2 (km s^{-1})$^{-3}$, with S + Irrs contributing 74 per cent of this density and E + S0s contributing the remaining 26 per cent. If this density is expressed in units of average-'luminosity' galaxies, the number density of these is 3.8×10^{-2} per $(h^{-1}$ Mpc$)^3$ for S + Irr galaxies and 1.3×10^{-2} per $(h^{-1}$ Mpc$)^3$ for E + S0 galaxies. The average density in the cloning strips adjacent to the zone of avoidance and to the missing equatorial strip is higher than the global mean. Because these strips are double-counted in the cloned mask model, the global mean density for this model is 10 per cent higher than that of the average mask model.

The total shot-noise error in the mean density is only 2–3 per cent. Although the density field errors quoted throughout this paper are shot-noise errors only, this is not the only source of error. For example, we estimate that a 1σ random error in the diameter function parameter D_L leads to an 8 per cent error in the mean density within 8000 km s^{-1}. The total error in the density of the local 8000 km s^{-1} sphere is therefore approximately 9 per cent.

Fig. 9 plots the density (in units of the mean density) and the shot-noise error in shells around the Local Group. Note that these shells are not of equal volume: the first shell extends from the Local Group to 1000 km s^{-1}, and subsequent shells have a thickness of 500 km s^{-1}. Fig. 9(a) shows the total catalogued area. The innermost shells sample essentially only one structure: the Virgo supercluster; more distant shells average over high- and low-density environments. While the optical density field is flat beyond Virgo in the distance range $2000 \lesssim r \lesssim 6500$ km s^{-1}, it shows a 17 ± 4 per cent drop in the range $6500 \lesssim r \lesssim 8000$ km s^{-1}. However, errors in the diameter functions affect the density most strongly in the outermost shells. We estimate that a 1σ random error in D_L causes a 15–20 per cent error in the density at 8000 km s^{-1} (depending on the diameter completeness).

Fig. 9(b) shows the density in the CfA1 (solid line), PP (dashed line) and unsurveyed UGC (dotted line) volumes.

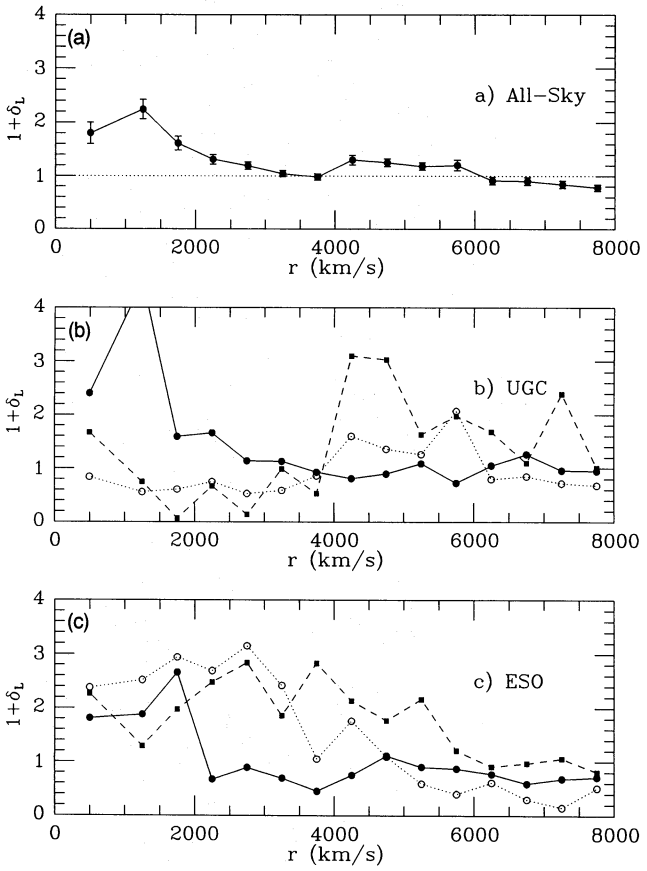

Figure 9. Density in shells around the Local Group. The first shell extends from 0 to 1000 km s^{-1}, and subsequent shells are 500 km s^{-1} thick. The density is in units of the mean density (average mask model). (a) The radial density run for the total catalogued area. The error bars indicate the shot-noise error only. The scatter expected due to clustering is not shown, but note that this affects the innermost shells most strongly, as these sample essentially a single structure: the Virgo supercluster. (b) The radial density run for the UGC area subdivided into the CfA1 (solid line), PP (dashed line) and unsurveyed (dotted line) areas. (c) The radial density run for the ESO area subdivided into the SSRS (solid line), SPS (dashed line) and unsurveyed (dotted line) areas.

Globally, the CfA1 volume is at the mean density $(1 + \delta_L = 1.03 \pm 0.04)$. The peak at $r = 1250$ km s^{-1} in the CfA1 survey is due to Virgo. The strong peaks at $r > 4000$ km s^{-1} is the PP area and in the unsurveyed area are due to the Perseus–Pisces supercluster. Fig. 9(c) shows the SSRS (solid line), SPS (dashed line) and unsurveyed ESO (dotted line) volumes. Note that the entire SSRS volume is underdense $(1 + \delta_L = 0.78 \pm 0.03)$, whereas the SPS volume is overdense $(1 + \delta_L = 1.37 \pm 0.07)$.

In Fig. 10 we show a 3D isodensity contour map of the density field (average mask model) smoothed with a 500 km s^{-1} Gaussian. Only features within 8000 km s^{-1} are shown. The Local Group lies at the centre of the box (indicated by an 'x'), with the North Galactic Pole towards the top of the box (the Z-axis). The X-axis is towards the Galactic Centre, and the Y-axis is in the direction of galactic rotation. The isodensity contour is set at $\delta_L = 1.5$. In Fig. 10(a) the viewpoint is from $l = 35°$, $b = 25°$, nearly perpendicular to the Supergalactic Plane. In Fig. 10(b) the viewpoint has been

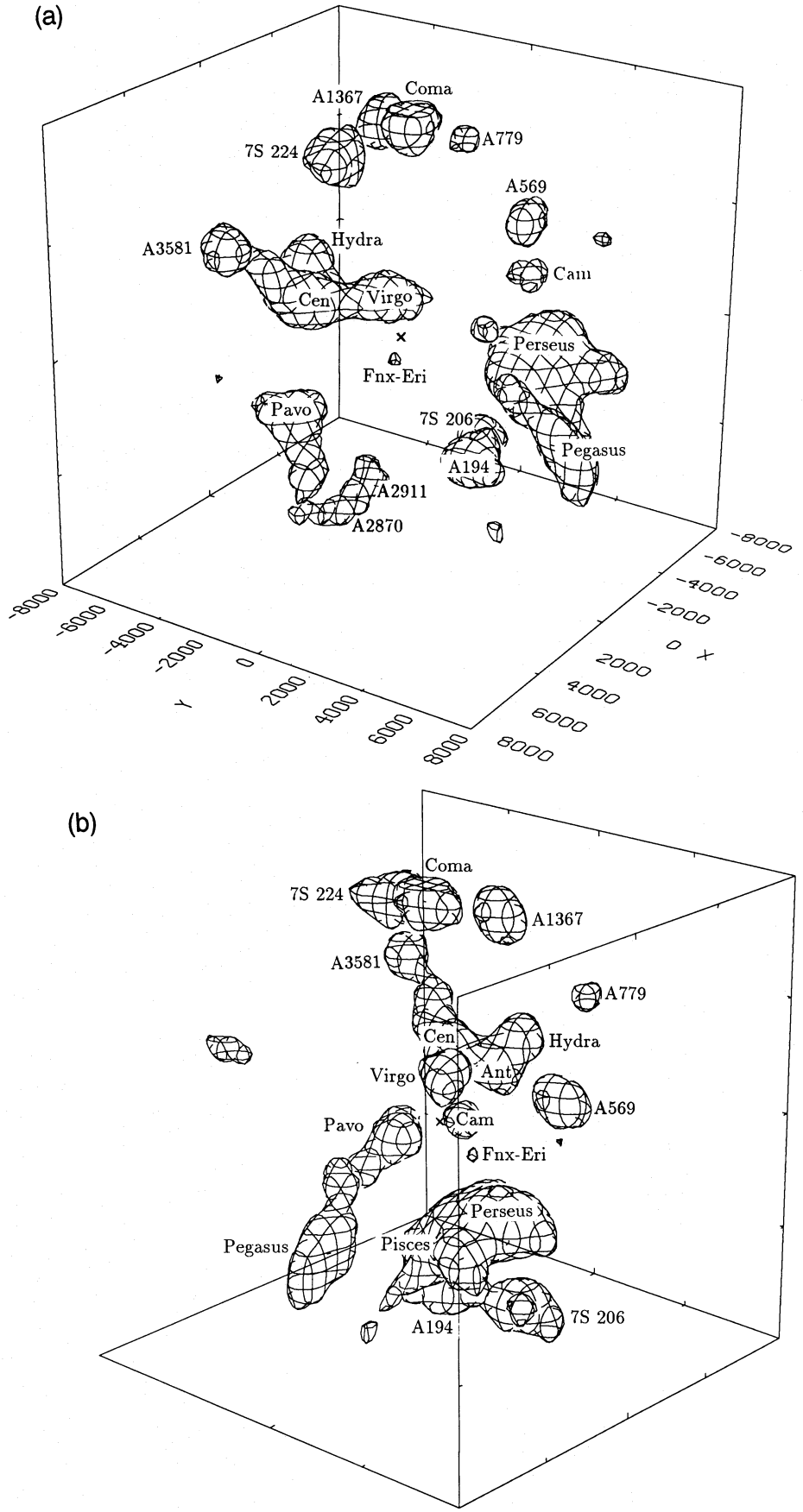

Figure 10. Three-dimensional isodensity contour plots of the local Universe. The density field (average mask model) has been smoothed with a 500 km s^{-1} Gaussian filter. Only features within 8000 km s^{-1} are shown. The Local Group lies at the centre of the plot (indicated by an 'x'), with the North Galactic Pole towards the top of the box (the Z-axis). The X-axis is towards the Galactic Centre and the Y-axis is in the direction of galactic rotation. Superclusters are labelled with the name of the nearest cluster or group. The isodensity contour is at $\delta_L = 1.5$. (a) The viewpoint is from $l = 35°$, $b = 25°$, nearly perpendicular to the Supergalactic Plane. (b) The viewpoint has been rotated by 90° in longitude so that it is almost aligned with the Supergalactic Plane; it is now from $l = 125°$, $b = 25°$. Note the concentration of superclusters towards the Supergalactic Plane.

rotated by 90°, so that it is now from $l = 125°$, $b = 25°$, almost in the Supergalactic Plane. Fig. 11 shows the density field (average mask model) in the Supergalactic Plane at 500 km s^{-1} Gaussian smoothing.

We discuss the overdensities of prominent superclusters in the volume in a more quantitative manner, and compare the predicted and measured supercluster infalls in detail in Section 9. We now turn to the comparison between the density fields of early- and late-type galaxies, and of optical and *IRAS* galaxies.

7 MORPHOLOGICAL SEGREGATION

It is well known that early-type galaxies are found preferentially in high-density environments (Dressler 1980). Giovanelli, Haynes & Chincarini (1986a) and Santiago & Strauss (1992) have investigated morphological segregation on large scales. Here we investigate the large-scale morphological segregation using the optical density fields of early- and late-type galaxies. We have calculated density fields for the E + S0 and S + Irr subsamples separately (average mask model), and binned the densities into cubical cells 2500 km s^{-1} wide. Fig. 12 shows the fraction of early-type galaxies, f_{E+S0}, against density $1 + \delta$ for all cells within 8000 km s^{-1} that have more than 75 per cent of their volume within the catalogued areas. Qualitatively, the fraction of early-type galaxies behaves in a manner similar to that described by Dressler (1980): the fraction of early-type galaxies increases from $\lesssim 10$ per cent in low-density cells to as high as ~ 40 per cent in high-density cells. Due to the large smoothing, however, the highest densities probed are much less than seen in the cores of rich clusters. The best-fitting straight line is a poor fit (rejected at > 99.9 per cent confidence level) due to some highly significant exceptions to the general trend. For example, the most discrepant cell includes the spiral-rich Ursa Major cluster but is underdense in early-type galaxies ($1 + \delta = 1.78 \pm 0.12$, $f_{E+S0} = 0.12 \pm 0.02$). This may be an example of a cluster that has yet to collapse and form cluster ellipticals.

8 OPTICAL AND *IRAS* DENSITY FIELDS

IRAS samples have been used to make predictions of the peculiar velocities of the Local Group and of other galaxies, from which values of β_I are deduced. It is therefore interesting to compare the optical and *IRAS* density fields, because differences in clustering (or the relative biasing) of the two populations will lead to different inferred values of β. We have used the 2-Jy redshift sample of Strauss et al. (1992c, kindly made available to us in machine-readable form by M. Strauss) to make quantitative comparisons between the optical and *IRAS* density fields. For convenience, we perform the comparison in redshift space. While this use of redshift space may cause some distortion, structures in both density fields should be distorted in the same sense. We have weighted the galaxies in the 2-Jy sample by the inverse of the *IRAS* selection function (Strauss et al. 1992a, hereafter SDYH), but using Local Group frame redshifts rather than (iterated) distances. The *IRAS* masked area and the Galactic Plane ($|b| < 5°$) are filled with random 'galaxies' at the average density. We have compared this to a redshift-space variant of the average mask model.

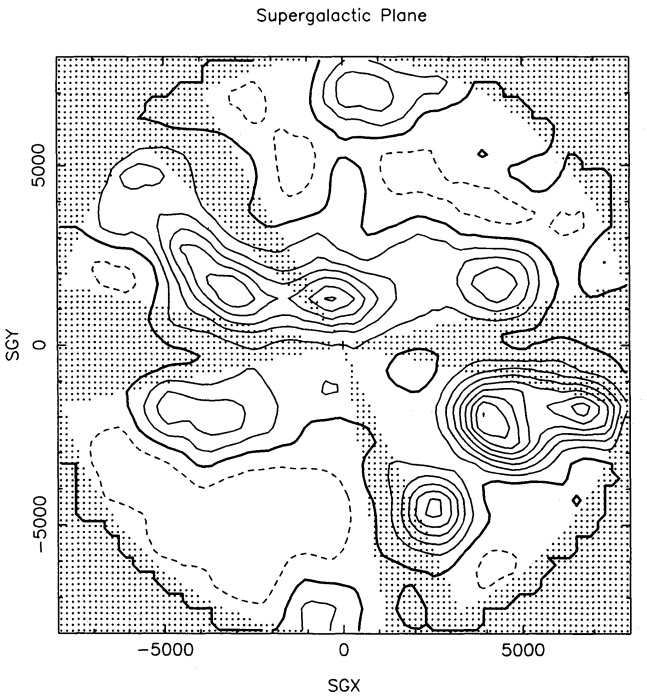

Figure 11. The density field (average mask model) in the Supergalactic Plane to 8000 km s^{-1}. The heavy line indicates the mean density and the dashed contours indicate densities below the mean. The masked area and volume beyond 8000 km s^{-1} are shaded. The density field has been smoothed with a 500 km s^{-1} Gaussian filter. The contour spacing is $\Delta\delta = 0.5$. Note that the overdensity in the Centaurus direction (second quadrant) extends to the edge of the plot. Coma and the nearer parts of the Great Wall appear at the top. In the fourth quadrant, the main ridge of the Perseus–Pisces supercluster runs perpendicular to this plane and peaks at the Perseus supercluster, which is below the plane (i.e. into the page).

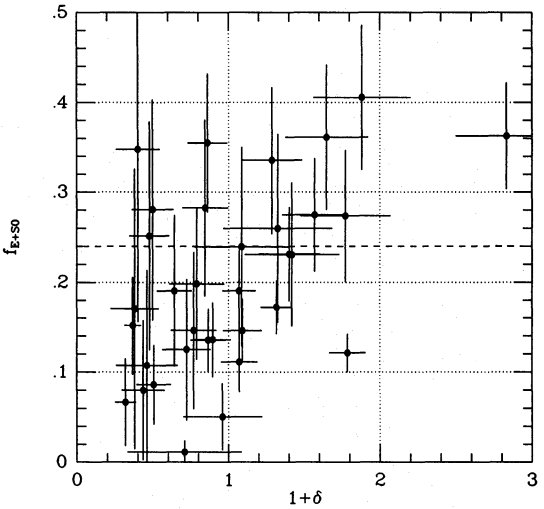

Figure 12. E + S0 fraction as a function of density, $1 + \delta$, in cells 2500 km s^{-1} wide. Only cells with more than 75 per cent of their volume within the catalogued volume are shown. The dashed line shows the average fraction. There is no straight line that is an acceptable fit to these data.

On the largest scales, we have compared the mean optical densities in the CfA1, SSRS and SPS volumes (with $r < r_{max} = 8000$ km s^{-1} and $|b| \geq 12°$) with the densities in the same volumes from the *IRAS* 2-Jy sample. For the CfA1, SSRS and SPS volumes the density of *IRAS* galaxies is 1.01 ± 0.08, 0.76 ± 0.07 and 1.16 ± 0.13, respectively, whereas we find 1.02 ± 0.04, 0.77 ± 0.03 and 1.27 ± 0.06, for the same volumes. The *IRAS* values differ slightly from those quoted by SDYH because we have normalized to the mean density in the catalogued area; our results differ slightly from those in Section 6 because the densities are in redshift space. Because *IRAS* galaxies are uniformly selected across the sky, this excellent agreement confirms that the UGC and ESO catalogues have been well matched by the completeness and diameter corrections adopted above. The optical density field shows a higher overdensity at $r \lesssim 2000$ km s^{-1} than the *IRAS* 2-Jy density field, but this difference can be accounted for in terms of the relative biasing of the two density fields on intermediate scales, as discussed below. At $r > 6000$ km s^{-1}, the optical density field drops slightly more ($1 + \delta_L = 0.87 \pm 0.04$) than the *IRAS* density field ($1 + \delta_I = 0.93 \pm 0.06$), but the difference is not significant.

Fig. 13 shows redshift-space density fields in the Supergalactic Plane of optical and 2-Jy galaxies, after smoothing with a 1000 km s^{-1} Gaussian. Qualitatively, the same structures (Centaurus–Hydra–Virgo–Pavo and Perseus–Pisces) appear in both plots, although the contrast of the optical maps is higher than that of the *IRAS* maps. In Fig. 14(a) we show the density in shells centred on the Local Group for the optical (solid line) and *IRAS* (dotted line) samples in the northern galactic ($b > 12°$) SPS volume. Fig. 14(b) covers the PP survey volume. Note that the optical density is generally enhanced with respect to the *IRAS* density, particularly at the high peaks near Cen 30 and in the Perseus–Pisces ridge, but that the Perseus–Pisces foreground void appears in both populations.

In Fig. 15, we plot the *IRAS* densities against the optical densities in 2500 km s^{-1} cells within 8000 km s^{-1} that have more than 75 per cent of their volume in the catalogued volume. (The volume of a 2500 km s^{-1} cell is equal to that of a 1550 km s^{-1} top-hat sphere or a 1000 km s^{-1} Gaussian filter.) We have fitted a straight line with an adjustable slope and zero-point to the data in Fig. 15, allowing for errors in both the optical and *IRAS* densities. The fit is shown as the solid line in Fig. 15. The χ^2 of the fit indicates that a straight line is an acceptable fit. Note, however, that, because there are some galaxies in common to both the optical and *IRAS* samples, the errors in the densities are not truly independent. The best-fitting slope of 0.74 ± 0.09 is an estimate of the relative linear bias, b_I/b_o, on these scales. This is in good agreement with the biasing ratio determined from comparisons of the correlation functions of optical and *IRAS* galaxies. A number of authors (e.g. Babul & Postman 1990; Lahav, Nemiroff & Piran 1990; Saunders, Rowan-Robinson & Lawrence 1992) have found *IRAS* correlation functions corresponding to rms fluctuations in an 800 km s^{-1} sphere of $\simeq 0.7$, whereas the canonical value for optical galaxies is unity (Davis & Peebles 1983).

We conclude that, on the largest scales, the optical and *IRAS* density fields are compatible, but that the optical density field shows larger fluctuations about the mean density than do the *IRAS* density fields in 2500 km s^{-1} cells by a factor of 1.35 ± 0.16.

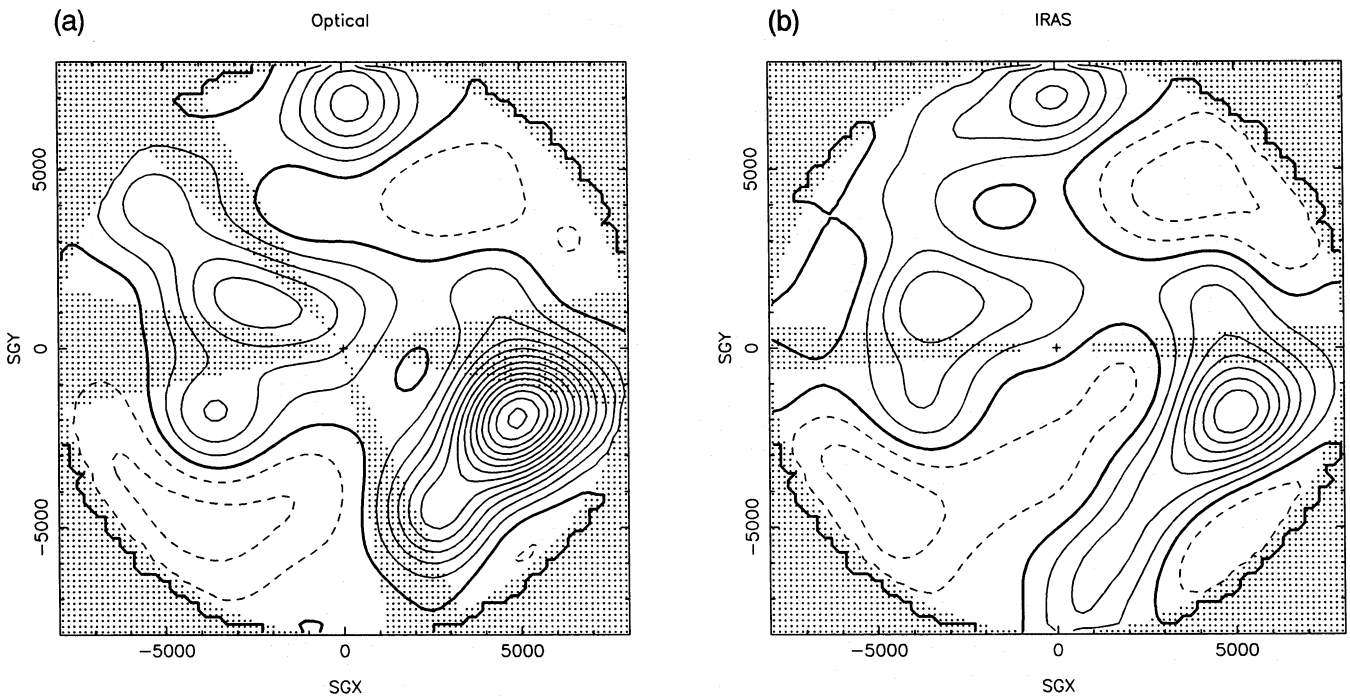

Figure 13. The Supergalactic Plane in Local Group redshift space after smoothing with a 1000 km s^{-1} Gaussian filter. The contour spacing is $\Delta\delta = 0.25$, the heavy contour indicates the mean density and the dashed contours indicate densities below the mean. (a) The density field of optical galaxies. The masked area and volume beyond 8000 km s^{-1} are shaded. (b) The density field of *IRAS* galaxies. The zone of avoidance ($|b| < 5°$) and volume beyond 8000 km s^{-1} are shaded.

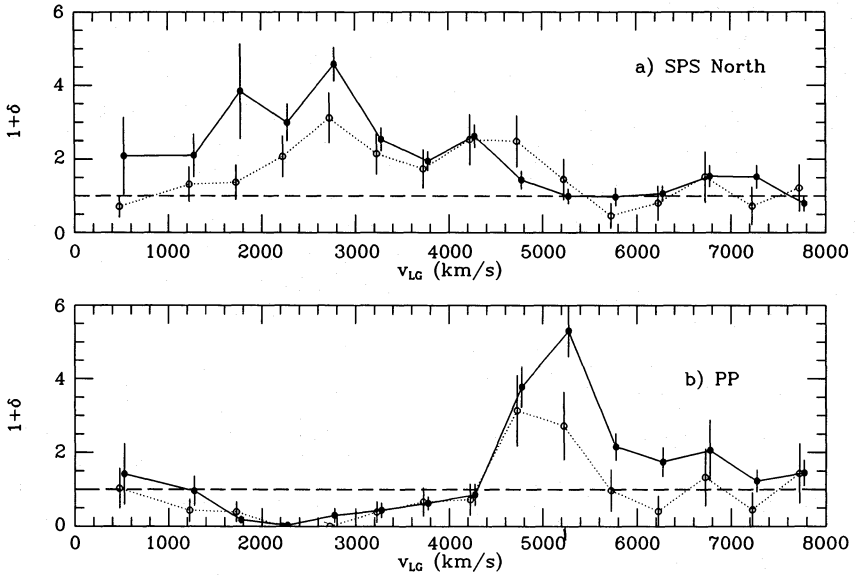

Figure 14. The density field in redshift-space shells centred on the Local Group. The optical density field is shown by the solid circles and lines; the *IRAS* 2-Jy density field is indicated by the dotted line and open symbols. The dashed line indicates the mean density. (a) The SPS volume at $b > 12°$. Note the overdensity of this volume and the prominent peak at Cen 30, and the secondary maximum at 7000 km s^{-1}. (b) The PP volume, which includes part of the main Perseus–Pisces ridge, but not the densest region near Perseus. Note that optical density shows higher contrast compared to the *IRAS* density, particularly at the ridge at 5000 km s^{-1}, and that the Perseus–Pisces foreground void appears in both populations.

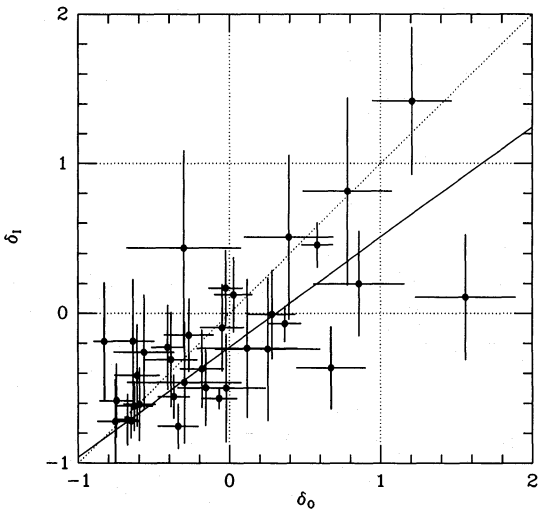

Figure 15. The *IRAS* overdensity plotted against the optical overdensity in redshift space. The densities are measured in cells 2500 km s^{-1} wide. Only cells with more than 75 per cent of their volume within the catalogued volume are shown. The solid line is the best fit to the $\delta_I - \delta_L$ relation, accounting for shot-noise errors in both density fields (assumed to be independent). A slope of 1 (dotted line) is excluded at a significance level of $\approx 3\sigma$.

9 SUPERCLUSTERS AND STREAMING MOTIONS

One of the ultimate goals of this work is a comparison between the overdensity of light around major superclusters and the infall patterns determined from peculiar velocities. Table 9 lists the maxima of the density field after smoothing it with 500 km s^{-1} and 1000 km s^{-1} Gaussian filters. In Table 9, these maxima have been labelled with the name of the nearest cluster(s). The superclusters may be grouped into four main complexes: Centaurus–Hydra–Virgo–Pavo; Perseus–Pisces and nearby superclusters Pegasus and A194–7S 206/A400, which form part of the 'Cetus Wall' (Fairall et al. 1990); A2870–A2911–DC 0237 − 31, which is part of the Sculptor Wall (da Costa et al. 1988; Fairall et al. 1990); and the nearer part of the Great Wall (Geller & Huchra 1989), comprising Coma–A1367–7S 224. Most of the Great Wall is excluded by the distance limit of 8000 km s^{-1}, as are other more distant superclusters, such as the Shapley Concentration (Raychaudhury 1989; Scaramella et al. 1989) and Hercules, which is prominent in the QDOT survey (S91).

If we assume that a given supercluster is spherically symmetric, and that the tidal influence of other superclusters is negligible, then, in linear theory, the infall peculiar velocity $u_{\rm inf}$ at a distance r from the centre of the supercluster is given by

$$u_{\rm inf} = \frac{\beta_o}{3}\,\overline{\delta}_{\rm L} r, \qquad (19)$$

where $\overline{\delta}_{\rm L}$ is the mean overdensity within r. Table 10 gives the mean overdensities within spheres that extend to the Local Group and are centred around a number of infall centres (described below), and the corresponding infall velocity at the distance of the Local Group. We now compare these predictions to the observed infall to these superclusters.

9.1 Virgo infall

The infall into the Virgo (Local) supercluster is the best determined as a result of its proximity to the Local Group. Huchra (1988) reviews this subject and concludes from the data of Aaronson et al. (1982) that Virgo 'pattern infall' is

Table 9. Superclusters.

500 km s^{-1} Gaussian Smoothing					1000 km s^{-1} Gaussian Smoothing				
Name	l	b	r	$1+\delta_L$	Name	l	b	r	$1+\delta_L$
Fornax/Eri	223	-54	1520	2.9±0.4					
Virgo	281	73	1380	4.5±0.4					
Cen/A3565	303	23	3490	5.6±0.5	Centaurus	299	26	2860	2.43±0.10
Antlia	273	20	3000	4.4±0.4					
Hydra	268	28	4200	4.8±0.6					
A3581	325	32	6670	4.3±0.9					
Pavo	334	-26	4300	4.6±0.5	Pavo	336	-25	4450	1.96±0.13
Perseus	151	-13	5870	20.6±4.9	Perseus	149	-14	5760	4.38±0.66
A262	141	-24	4400	6.0±0.7					
Pisces	130	-29	5080	5.6±0.7					
Pegasus	94	-21	6390	3.9±1.2	Pegasus	96	-26	7780	2.12±0.35
A194	142	-61	5180	6.4±1.1	A194	143	-60	5400	2.19±0.21
7S 206/A400	167	-52	6280	7.0±1.6					
Cam	141	21	4560	3.1±0.5					
A569	168	22	6300	4.9±1.0	A569	168	21	6300	1.66±0.22
A779	190	44	7170	3.2±1.1					
A2870	288	-72	6480	3.4±0.7	Sculptor Wall	298	-66	7920	1.53±0.28
A2911	261	-78	5620	2.9±0.4					
DC0237-31	228	-64	6360	2.8±0.7					
A1367	234	74	6780	6.6±1.7					
7S 224	339	72	7160	4.1±1.1	1352+9	345	67	7970	2.63±0.48
Coma	72	88	7320	6.5±1.4	Coma	100	88	7990	2.92±0.45

Table 10. Overdensities in spheres and predicted Local Group infall.

	Sphere centre			Cloned Mask model		Average Mask model	
	l	b	r	$\overline{\delta_L}$	$u_{\rm inf}/\beta_o$ km s^{-1}	$\overline{\delta_L}$	$u_{\rm inf}/\beta_o$ km s^{-1}
Virgo	281	73	1380	1.70±0.20	784±94	1.54±0.20	709±93
Fnx-Eri	223	-54	1520	0.35±0.14	178±69	0.29±0.14	147±71
GA1	307	9	4350	0.16±0.10	234±140	0.20±0.10	283±139
GA2	309	18	4200	0.29±0.10	376±136	0.29±0.10	406±136
Cen30	303	23	3490	0.45±0.10	525±115	0.37±0.10	434±115
Perseus-Pisces	127	-30	5500	0.23±0.10	428±189	0.09±0.10	161±181

250 ± 64 km s^{-1} at the Local Group. Davis & Huchra (1982) found the overdensity of Virgo within the sphere extending to the Local Group to be $\overline{\delta}_{\rm Virgo} = 2.0 \pm 0.2$, although this estimate was restricted to the high galactic latitudes ($|b| > 40°$) covered by the CfA1 survey. The cloned mask model density field (smoothed on a scale of 500 km s^{-1}) peaks at $r = 1380$ km s^{-1}, about 100 km s^{-1} beyond the distance of the Virgo cluster itself. We adopt this peak as the centre of overdensity in Virgo. The overdensity and the motion of the Local Group predicted by equation (19) are shown in Table 10. Although the good agreement with the results of Davis & Huchra is not surprising, considering we used the same CfA1 data, it demonstrates that our diameter-based methods are consistent with luminosity-based methods. Comparing the predicted infall from Table 10 to Huchra's infall value, we obtain, for the cloned mask model, $\beta_o = 0.32 \pm 0.09$, or $\Omega = 0.15 \pm 0.07$ if $b_o = 1$ (the results are 0.35 and 0.17 respectively for the average mask model). However, if we were to use non-linear theory (e.g. Nusser et al. 1991) and assume $b_o = 1$, we would infer $\Omega = 0.23$ ($\beta_o = 0.41$) for the cloned mask model.

Note, however, that the Virgo supercluster is not spherically symmetric, but is flattened towards the Supergalactic Plane and, within the Supergalactic Plane, is concentrated towards the Ursa Major–Centaurus axis (see Fig. 8). The effect of a flattened distribution on infall in the Supergalactic Plane depends on the flattening and density of the shells inside *and outside* the shell containing the Local Group: if the flattening extends beyond the Local Group, then the infall will be reduced compared to the prediction of the spherical infall model, whereas if the Local Group lies at the edge of the Supergalactic Plane then the infall should be stronger (Hoffman & Salpeter 1982; Szalay & Silk 1983; Villumsen & Davis 1986). The tidal shear of external superclusters might also affect Virgo infall. For example, from Table 10, the effect of Fornax–Eridanus on the Local Group is $\approx 170\ \beta_o$ km s^{-1}, which may decrease the predicted infall and hence increase the estimate of β_o by as much as 30 per cent. Furthermore, Hydra–Centaurus (Lilje, Yahil & Jones 1986) and/or the Great Attractor (FB88) or the Local Void (Yahil 1990) might also have tidal fields strong enough to affect Virgo infall.

N-body simulations of superclusters resembling the Local Supercluster indicate that errors in the apparent values of Ω from the application of the spherical infall model are likely to be large: a factor of 2 or more (Bushouse et al. 1985); a factor of 3 (Villumsen & Davis 1986); or a 20 per cent random error and Ω systematically low by 20–40 per cent (Lee, Hoffman & Ftaclas 1986). Considering the wide range of observational and modelling uncertainties, we shall assume that β_0 lies in the range 0.15–0.65 (or $\Omega = 0.05$–0.50 if $b_0 = 1$). None the less, even such weak constraints are useful in predicting the infall towards Centaurus–Hydra.

9.2 Centaurus–Hydra

The Centaurus–Hydra region is of particular interest due to its proximity to the direction of the Local Group's motion in the CMB frame and to the location of the proposed Great Attractor inferred from peculiar velocity surveys (7S). Fig. 9(c) shows that the SPS region defined by Dressler ($290° < l < 350°$, $-35° < b < 45°$) is denser than the mean in the distance range $1500 \leq r \leq 6000$ km s^{-1} and is globally ($0 < r < 8000$ km s^{-1}) overdense by 37 ± 7 per cent. In the galactic north, the highest density peak is at $r = 3490$ km s^{-1}, the distance of the Cen 30 and A3565 clusters (which are not resolved at 500 km s^{-1} Gaussian smoothing), with somewhat lower peaks at Hydra and Antlia. The region in the galactic north centred on Klemola 27 (= A3574) was identified by 7S as a likely candidate for the Great Attractor (this region is referred to as 'North Centaurus' by RR90 and S91 and as the 'Centaurus Concentration' by Lynden-Bell et al. 1989). We do not, however, find a *maximum* in the galactic north at 4500 km s^{-1} (see also Fig. 4a), although the density field is still significantly overdense there: $1 + \delta_L = 3.37 \pm 0.50$. In Fig. 10, the Virgo supercluster merges with the Centaurus–Hydra supercluster, and should properly be considered to be part of this supercluster complex, as noted by authors using *IRAS* samples (RR90; S91; SDYH). Fig. 10 shows the supercluster complex in Centaurus to be an overdense ($1 + \delta_L \geq 2.5$) cylindrical structure, extending approximately along the line of sight from Virgo, through a maximum at the Cen 30 cluster at $r = 3490$ km s^{-1}, to a secondary maximum with density $1 + \delta_L = 4.3 \pm 0.9$ at $l = 325°$, $b = 32°$ and $r = 6670$ km s^{-1}, which is near the cluster A3581. In the galactic south, there is a prominent maximum in Pavo at $r = 4300$ km s^{-1}. It seems likely that the Pavo supercluster is part of the same complex as Centaurus, as both of these superclusters are overdense until they disappear on opposite sides of the zone of avoidance. Thus, while there is no obvious maximum at the proposed location of the Great Attractor, the Centaurus–Hydra–Virgo–Pavo supercluster complex is clearly an extended region of overdensity of dimensions ≈ 6000 km s^{-1} along the Virgo–A3581 axis.

Assuming that fluctuations in mass are proportional to fluctuations in light, is this region sufficiently overdense to account for the motion of the Local Group and the streaming towards the Great Attractor? 7S estimate that the sphere centred on $r = 4350$ km s^{-1} and extending to the Local Group must have an overdensity of 0.4, if mass traces light and $\Omega = 1$, to account for the observed streaming motions. From Table 10 (the row labelled 'GA1'), the overdensity of the sphere centred on the Great Attractor is only 0.16–0.20 ± 0.10. Thus, even if $\beta_0 = 1$, *this sphere is not sufficiently overdense to fit the Great Attractor model.* Furthermore, $\beta_0 = 1$ is inconsistent with the determinations from Virgo infall discussed above. The revised Great Attractor model of Faber & Burstein (1988; labelled 'GA2' in Table 10) fares somewhat better, but still falls short for values of β consistent with Virgo infall, which in Faber & Burstein's model is only 85–115 km s^{-1}.

The assumption of spherical symmetry is not, however, a good one: there are five local maxima (one of which is Virgo) within the Great Attractor spheres. The most prominent maximum is at the Cen 30 cluster, and this is closer than are the Great Attractor model centres to the centre of mass of the overdense region. Table 10 also indicates that the pull from a sphere centred around the Cen 30 density peak is greater than that from either of the Great Attractor models. Unless there is a massive supercluster hidden in the zone of avoidance, over and above that provided by our cloning procedure, *the optical density field predicts* local *infall into or just behind Cen 30 at* $r = 3000$–3500 km s^{-1}, *and not into an attractor at* $r = 4200$–4350 km s^{-1}. From Table 10, the predicted ratio of Cen 30 infall to Virgo infall at the Local Group is well determined (0.64 ± 0.18, averaging the cloned and average mask models), but the absolute value of Cen 30 infall depends on the uncertain value of β_0 deduced from the Virgo infall comparisons. Taking $\beta_0 = 0.4 \pm 0.25$, the Local Group's infall into Cen 30 is then 200 ± 125 km s^{-1}. While this prediction disagrees with the Great Attractor infall models of 7S and FB88, it is in better agreement with the results of Staveley-Smith & Davies (1989) in terms of the location of the infall centre. The predicted amplitude of infall does not, however, agree with their results unless $\beta_0 = 0.75$–1.15, which is again inconsistent with Virgo inflow.

These results indicate that the outward streaming in the CMB frame of Cen 30, and galaxies beyond it in Centaurus, must be due to sources outside the mapped volume. This suggests that a flow model with weak infall into Centaurus plus a bulk dipole motion of 400 ± 150 km s^{-1} in a similar direction may provide a better fit to the observed streaming motions. In the Hubble diagram towards Centaurus (e.g. fig. 2b of Dressler & Faber 1990a), this bulk motion would add a constant offset, shifting a (weak) Centaurus infall curve ('S-curve') upwards, and thus moving the zero-crossing to a greater distance. The backside infall would then be weak or non-existent depending on the relative strengths of the bulk motion and the infall component. The existence of backside infall is unresolved. Dressler & Faber (1990a,b) claim to have detected backside infall. On the other hand, the results of Mathewson, Ford & Buchhorn (1992a,b), particularly when considered in the light of the Perseus–Pisces peculiar velocity surveys of Willick (1990), Courteau (1992) and Han & Mould (1992), argue against an infall model and in favour of a bulk motion.

9.3 Perseus–Pisces

The densest maximum in the volume ($l = 149°$, $b = -14°$, $r = 5760$ km s^{-1} in the average mask model) is coincident with the Perseus cluster. The main ridge of the Perseus–Pisces supercluster is overdense from its peak at Perseus through A347, A262 and the Pisces cluster(s). We

also identify a supercluster in the vicinity of the clusters A194 and 7S 206, and a lower density enhancement in Pegasus (which is distinct from the nearer Pegasus cluster). Both of these superclusters are connected to the main ridge at lower overdensities (see also fig. 4 of Giovanelli et al. 1986a).

We caution that, near Perseus, the random and systematic errors are high due to the generally low and patchy redshift completeness, and the fact that Perseus is in a region of high galactic absorption (0.68 mag from Burstein & Heiles 1982). Perseus is also the highest peak within 8000 km s^{-1} in the *IRAS* 2-Jy and QDOT maps. S91 found $1+\delta_I = 3.08 \pm 0.63$ (1000 km s^{-1} Gaussian smoothing), whereas we find $1+\delta_L = 4.38 \pm 0.66$. These values are consistent if optical galaxies are relatively more 'biased' compared to *IRAS* galaxies by a factor ≈ 1.4, as discussed in Section 8 above. This good agreement argues against systematic errors in the optical maps being much larger than the random errors.

In Table 10, we list the estimated infall at the Local Group from the Perseus–Pisces supercluster (the centre of which we take to be the Pisces cluster). However, the infall depends strongly on the interpolation into the zone of avoidance. For example, in the cloned mask model the Perseus cluster and A347 are double-counted. If we assume that Perseus is the densest region of this supercluster, but that the main ridge does continue into the zone of avoidance, then a better model might be the average of the cloned and average mask models. We then obtain a predicted Perseus–Pisces infall of $(295 \pm 180)\ \beta_o$ km s^{-1} at the Local Group. Note, however, that the assumption of spherical symmetry is not a good one here either: the main ridge is a filament perpendicular to the line of sight. More important in terms of the pull on the Local Group itself is the effect of the void between the Local Group and Perseus–Pisces. The push on the Local Group from this foreground void will be underestimated in this assumption, hence the net pull on the Local Group from this direction is probably overestimated. Thus, while Perseus–Pisces is the dominant structure in the volume, its geometry, the foreground void and its greater distance from the Local Group result in its effect on the Local Group being weaker than that of Centaurus–Hydra, whose overdensity extends closer to the Local Group. The Local Void will also have an important effect on the motion of the Local Group (Lynden-Bell & Lahav 1988). The result is that Centaurus–Hydra beats Perseus–Pisces in the 'tug-of-war' on the Local Group. This is in agreement with the statement of Yahil (1988) based on the 2-Jy survey; he claimed that the 'gravitational field shows a bifurcation between these two great complexes, not far from the Local Group' (in the direction of Perseus–Pisces).

None the less, strong infall closer to the Perseus–Pisces supercluster is predicted from the optical density field. Staveley-Smith & Davies (1989) fitted a cluster-centred infall model to their Tully–Fisher peculiar velocity data: they found that, at the distance of the Local Group, the infall into Perseus is 645 ± 199 km s^{-1}, whereas the infall into Pisces is -367 ± 195 km s^{-1}. Since the latter is unphysical, fixing it to be zero they obtained a Perseus–Pisces infall of 350 ± 200 km s^{-1}. Han & Mould (1992) have obtained *I*-band Tully–Fisher peculiar velocities for 21 clusters. Their best-fitting model has two infall centres. The first of these is at $r = 7000$ km s^{-1} and $l = 307°$, $b = 51°$ and has an infall of 497 ± 57 km s^{-1} at the Local Group. (Note that this is quite different from the Great Attractor models of 7S and FB88 in galactic latitude and in distance.) Nearby, this infall will be very similar to a bulk flow because the tidal field falls off like r^{-3}. Their other centre is fixed at Pisces at $l = 130°$, $b = -30°$. The best-fitting distance is $r = 4851$ km s^{-1}, and the infall is 100 ± 48 km s^{-1} at the Local Group. Taken together, these results indicate that there is indeed infall into Perseus–Pisces as expected from the optical maps, although the amplitude of this infall is highly uncertain. This uncertainty, plus the discrepancy between the cloned and average mask models due to the uncertain extrapolation into the zone of avoidance and the large random error, make it difficult to place useful constraints on β_o from Perseus–Pisces infall. Combining the infall values of Staveley-Smith & Davies (1989) and Han & Mould (1992), and comparing this to the average of the average mask and cloned mask model predictions, we obtain $\beta_o = 0.42 \pm 0.26$, compatible with our results for Virgo infall. We also note that Courteau (1992) and Gavazzi et al. (1992) claimed to have detected infall into Perseus–Pisces based on additional scatter in the Tully–Fisher distances, but it is difficult to use their results in a quantitative comparison here.

9.4 Other superclusters

Infall into the Sculptor Wall and the Cetus Wall is predicted, although the amplitude will be much less than that of the Perseus–Pisces infall.

At high northern galactic latitudes, the nearer parts of the 'Great Wall' (Geller & Huchra 1989) are apparent with maxima at Coma, A1367 and the 7S group 224. The latter can be seen in fig. 3(d) of Geller & Huchra at RA = 13^h30, Dec. = +12. Note, however, that most of the 'Great Wall' is beyond the distance limit of 8000 km s^{-1}. Many more peculiar velocities will have to be obtained in this region before infall into this structure can be compared to predictions.

10 SUMMARY

Our main results are as follows.

(1) The optical density field is dominated by superclusters that are connected at lower overdensities to form extended, multimodal supercluster complexes. The most prominent of these complexes within 8000 km s^{-1} are Perseus–Pisces and Centaurus–Hydra–Virgo–Pavo.

(2) The density field of optical galaxies shows the same structures as *IRAS* density fields, although the fluctuations about the mean density are greater for optical than for *IRAS* galaxies by a factor of 1.35 ± 0.16 when measured in 2500 km s^{-1} cells. Due to this effect the inferred values of β_o are expected to be lower than the *IRAS* estimates of β_I by a similar factor due to the relative biasing of the populations.

(3) The overdensity of the Virgo (Local) Supercluster is 1.70 ± 0.2. Comparing this to Virgo infall, while allowing for non-linear effects and a wide range of possible tidal effects, we estimate $\beta_o = 0.4 \pm 0.25$ or $\Omega = 0.20^{+0.30}_{-0.15}$, if mass traces light.

(4) The overdensity centred about the proposed location of the Great Attractor is insufficient to account for the

infall motion found by 7S, unless there is a massive supercluster in the zone of avoidance. The higher overdensity in a sphere centred on the density field peak near the Cen 30 cluster indicates that this position is closer to the centre of the local infall pattern. The optical density field suggests that a flow model with a weak infall into Cen 30 of 200 ± 150 km s^{-1} (for consistency with Virgo infall) plus a bulk flow of 400 ± 150 km s^{-1} in a similar direction may provide a better fit to the observed large-scale streaming motions.

(5) Strong infall into the Perseus–Pisces supercluster is expected, although its greater distance and the foreground void reduce its effect at the Local Group to less than that of the Centaurus–Hydra–Virgo–Pavo complex.

The comparisons between predicted infall and observations, and the resulting estimates of β_o, are based on simple spherical infall models and are subject to uncertainties due to modelling of the 'pattern infall' and the tidal effects of external superclusters. A better method is to predict the peculiar velocities of the Local Group, and of individual galaxies with $D_n - \sigma$ or Tully–Fisher distances, using linear theory and the full density field within 8000 km s^{-1}. These comparisons will be the subject of future work.

ACKNOWLEDGMENTS

This paper presents part of my PhD thesis at the University of Cambridge. I am grateful to Donald Lynden-Bell for discussions and useful suggestions throughout the course of this project. This work rests largely upon the catalogues compiled through the diligent efforts of John Huchra, Tony Fairall, who is thanked for providing a copy of the SRC prior to its release, and Dave Burstein, who is thanked for discussions. Michael Strauss is thanked for providing a machine-readable version of the *IRAS* 2-Jy survey prior to publication. Caleb Scharf is thanked for running his spherical harmonics analysis software to generate Fig. 6. The hospitality of Hebrew University of Jerusalem, the Royal Observatory at Edinburgh and the University of Wales, College of Cardiff and the support of the NSERC of Canada, the FCAR of Québec, the Cambridge Commonwealth Trust and an ORS award are gratefully acknowledged.

REFERENCES

Aaronson M., Huchra J. P., Mould J. R., Schechter P. L., Tully R. B., 1982, ApJ, 258, 64
Auman J. R., Hickson P., Fahlman G. G., 1989, PASP, 101, 859
Babul A., Postman M., 1990, ApJ, 359, 280
Bothun G., Beers T., Mould J., Huchra J., 1985, AJ, 90, 2487
Burstein D., Heiles C., 1982, AJ, 87, 1165
Burstein D., Haynes M. P., Faber S. M., 1991, Nat, 353, 515
Bushouse H., Melott A. L., Centrella J., Gallagher J. S., 1985, MNRAS, 217, 7P
Choloniewski J., 1991, MNRAS, 250, 486
Cornell M. E., Aaronson M., Bothun G. D., Mould J., 1987, ApJS, 64, 507
Corteau S., 1992, PhD thesis, Univ. California, Santa Cruz
da Costa L. N., Willmer C., Pellegrini P. S., Chincarini C., 1987, AJ, 93, 1338
da Costa L. N. et al., 1988, ApJ, 327, 544
da Costa L. N., Pelligrini P. S., Davis M., Meiksin A., Sargent W. L. W., Tonry J. L., 1991, ApJS, 75, 935
Davis M., Huchra J., 1982, ApJ, 254, 437
Davis M., Peebles P. J. E., 1983, ApJ, 267, 475
Davis M., Strauss M. A., Yahil A., 1991, ApJ, 372, 394
de Vaucouleurs G., Pence W. D., 1978, AJ, 83, 1163
de Vaucouleurs G., de Vaucouleurs A., Corwin H. G., 1976, Second Reference Catalogue of Bright Galaxies. Univ. Texas Press, Austin (RC2)
de Vaucouleurs G., de Vaucouleurs A., Corwin H. G., Buta R. J., Paturel G., Fouqué P., 1991, Third Reference Catalogue of Bright Galaxies, Vol. I. Springer-Verlag, New York (RC3)
Dressler A., 1980, ApJ, 236, 351
Dressler A., 1991, ApJS, 75, 241 (SPS)
Dressler A., Faber S. M., 1990a, ApJ, 354, 13
Dressler A., Faber S. M., 1990b, ApJ, 354, L45
Faber S. M., Burstein D., 1988, in Coyne G., Rubin V. C., eds, Proceedings of the Vatican Study Week, Large Scale Motions in the Universe. Princeton Univ. Press, Princeton, p. 135
Fairall A. P., Jones A., 1991, Southern Redshift Catalogue, Publ. Dept. Astron., Univ. Cape Town, 1991, No. 11 (SRC)
Fairall A. P., Palumbo C. G. C., Vettolani G., Kauffmann G., Jones A., Baiesi-Pillastrini G., 1990, MNRAS, 247, 21P
Gavazzi G., Scodeggio M., Boselli A., Trinchieri G., 1992, A&A, 258, 265
Geller M. J., Huchra J. P., 1989, Science, 246, 897
Giovanelli R., Haynes M. P., 1984, AJ, 89, 1
Giovanelli R., Haynes M. P., 1985, AJ, 90, 2445 (PP)
Giovanelli R., Haynes M. P., Chincarini G., 1986a, ApJ, 300, 77
Giovanelli R., Haynes M. P., Myers S., Roth J., 1986b, AJ, 92, 250 (PP)
Han M., Mould J. R., 1992, ApJ, 396, 453
Helou G., Madore B. F., Schmitz M., Bicay M. D., Wu X., Bennett J., 1991, in Albrecht M. A., Egret D., eds, Databases and On-line Data in Astronomy. Kluwer, Dordrecht, p. 89
Hoffman G. L., Salpeter E. E., 1982, 263, 485
Huchra J. P., 1988, in van den Bergh S., Pritchet C. J., eds, ASP Conf. Ser. No. 4, The Extragalactic Distance Scale. Astron. Soc. Pac., San Francisco, p. 257
Huchra J. P., 1990, ZCAT, privately circulated
Huchra J. P., Geller M. J., 1982, ApJ, 257, 423
Huchra J., Davis M., Tonry J., Latham D., 1983, ApJS, 52, 89
Huchra J. P., Geller M. J., de Lapparent V., Corwin H. G., 1990, ApJS, 72, 433
Hudson M. J., 1992, PhD thesis, Univ. Cambridge
Hudson M. J., Lynden-Bell D., 1991, MNRAS, 252, 219 (HL-B)
Huizinga J. E., van Albada T. S., 1992, MNRAS, 254, 677
Kaiser N., 1987, MNRAS, 227, 1
Kaiser N., Lahav O., 1988, in Coyne G., Rubin V. C., eds, Proceedings of the Vatican Study Week, Large Scale Motions in the Universe. Princeton Univ. Press, Princeton, p. 339
Kaiser N., Efstathiou G., Ellis R., Frenk C., Lawrence A., Rowan-Robinson M., Saunders W., 1991, MNRAS, 252, 1
Kron E. G., Shane C. D., 1976, Ap&SS, 39, 401
Lahav O., Nemiroff R. J., Piran T., 1990, ApJ, 350, 119
Lauberts A., 1982, The ESO–Uppsala Survey of the ESO(B) Atlas. European Southern Observatory, Garching bei München (ESO)
Lee H., Hoffman Y., Ftaclas C., 1986, ApJ, 304, L11
Lilje P. B., Yahil A., Jones B. J. T., 1986, ApJ, 307, 91
Lynden-Bell D., Lahav O., 1988, in Coyne G., Rubin V. C., eds, Proceedings of the Vatican Study Week, Large Scale Motions in the Universe. Princeton Univ. Press, Princeton, p. 208
Lynden-Bell D., Faber S. M., Burstein D., Davies R. L., Dressler A., Terlevich R. J., Wegner G., 1988, ApJ, 326, 19 (7S)
Lynden-Bell D., Lahav O., Burstein D., 1989, MNRAS, 241, 325
Mathewson D., Ford V. L., Buchhorn M., 1992a, ApJ, 389, L5
Mathewson D., Ford V. L., Buchhorn M., 1992b, ApJS, 81, 413
Moore B., Frenk C., White S. D. M., 1993, MNRAS, 261, 827
Nilson P., 1973, Uppsala General Catalogue of Galaxies, Uppsala Astron. Obs. Ann., 6 (UGC)

Nusser A., Dekel A., Bertschinger E., Blumenthal G. R., 1991, ApJ, 379, 6
Paturel G., Fouqué P., Lauberts A., Valentijn E. A., Corwin H. G., de Vaucouleurs G., 1987, A&A, 184, 86
Paturel G., Fouqué P., Bottinelli L., Gouguenheim L., 1989, Monographies de la Base de Données Extragalactiques No. 1, Catalogue of Principal Galaxies. Observatoire de Lyon, Saint-Genis-Laval
Paturel G., Fouqué P., Buta R., Garcia A. M., 1991, A&A, 243, 319
Peebles P. J. E., 1980, The Large Scale Structure of the Universe. Princeton Univ. Press, Princeton
Raychaudhury S., 1989, Nat, 342, 251
Richter O.-G., 1987, A&AS, 67, 237
Richter O.-G., Materne J., Huchtmeier W. K., 1982, A&A, 111, 193
Rood H., 1991, Catalogue of Cluster Redshifts. Privately circulated
Rowan-Robinson M. et al., 1990, MNRAS, 247, 1 (RR90)
Sandage A., Perelmuter J.-M., 1990, ApJ, 361, 1
Sandage A., Tammann G., 1981, The Revised Shapley–Ames Catalog. Carnegie Institution of Washington, Washington
Santiago B. X., Strauss M. A., 1992, ApJ, 387, 9
Saunders W. et al., 1991, Nat, 349, 32 (S91)
Saunders W., Rowan-Robinson M., Lawrence A., 1992, MNRAS, 258, 134
Scaramella R., Baiesi-Pillastrini G., Chincarini G., Vettolani G., Zamorani G., 1989, Nat, 338, 562
Scharf C., Hoffman Y., Lahav O., Lynden-Bell D., 1992, MNRAS, 256, 229
Schmidt K.-H., 1986, Astron. Nachr., 307, 80
Shaya E. J., 1984, ApJ, 280, 470
Shaya E. J., Tully R. B., Pierce M. J., 1992, ApJ, 391, 16
Staveley-Smith L., Davies R. D., 1989, MNRAS, 241, 787
Strauss M. A., Davis M., Yahil A., Huchra J. P., 1990, ApJ, 361, 49
Strauss M. A., Davis M., Yahil A., Huchra J. P., 1992a, ApJ, 385, 421 (SDYH)
Strauss M. A., Yahil A., Davis M., Huchra J. P., Fisher K., 1992b, ApJ, 397, 395
Strauss M. A., Huchra J. P., Davis M., Yahil A., Fisher K., Tonry J., 1992c, ApJS, 83, 29
Szalay A. S., Silk J., 1983, ApJ, 264, L31
Tully R. B., 1988, Nearby Galaxies Catalog. Cambridge Univ. Press, Cambridge
Tully R. B., Fisher J. R., 1977, A&A, 54, 661
van den Bergh S., 1989, A&AR, 1, 111
Villumsen J. V., Davis M., 1986, ApJ, 308, 499
Vorontsov-Velyaminov B. A., Krasnogorskaya A., 1962, Morphological Catalogue of Galaxies, Part 1. Moscow State University, Moscow
Vorontsov-Velyaminov B. A., Arkhipova V. P., 1963–68, Morphological Catalogue of Galaxies, Parts 2–4. Moscow State University, Moscow
Weinberg S., 1972, Gravitation and Cosmology. Wiley, New York
Willick J. A., 1990, ApJ, 351, L45
Yahil A., 1988, in Coyne G., Rubin V. C., eds, Proceedings of the Vatican Study Week, Large Scale Motions in the Universe. Princeton Univ. Press, Princeton, p. 219
Yahil A., 1990, in Alimi J.-M., Blanchard A., Bouguet A., Martin de Volnay F., Tran Thanh Van J., eds, Proc. XXV Rencontre de Moriond, Particle Astrophysics: The Early Universe and Cosmic Structures. Editions Frontières, Gif-sur-Yvette, France, p. 483
Yahil A., Sandage A., Tammann G. A., 1980, ApJ, 242, 448
Yahil A., Strauss M. A., Davis M., Huchra J. P., 1991, ApJ, 372, 380 (YSDH)
Zwicky F., Herzog W., Wild P., Karpowicz M., Kowal C., 1961–68, Catalogue of Galaxies and of Clusters of Galaxies. California Institute of Technology, Pasadena (CGCG)